UNIVERSIDADE FEDERAL DE MINAS GERAIS
INSTITUTO DE CIÊNCIAS EXATAS

DÉBORAH REIS ALVARENGA

A Study on the Physical Properties of Quantum Dot Structures for Infrared Photodetection

Belo Horizonte - MG - Brasil
2011

DÉBORAH REIS ALVARENGA

A Study on the Physical Properties of Quantum Dot Structures for Infrared Photodetection

Tese apresentada ao Instituto de Ciências Exatas da Universidade Federal de Minas Gerais para obtenção do título de Doutor em Física.

Área de concentração: Física do Estado Sólido

Orientador: Paulo Sérgio Soares Guimarães

Co-orientadora: Patrícia Lustoza Souza

Belo Horizonte - MG - Brasil

2011

Essa tese é dedicada à nossa querida Princesa. Sua presença é amor, paz e alegria!

AGRADECIMENTOS

Em primeiríssimo lugar agradeço à minha família. Sem o apoio e o amor de vocês essa tese nunca existiria.

Ao meu orientador Paulo Sérgio, não apenas pela orientação dessa tese, mas pela amizade e carinho.

Aos professores Patrícia L. Souza, Wagner Nunes Rodrigues e Maurício Pamplona Pires pela co-orientação.

Ao Professor Karl Unterrainer e a todo o grupo da Universidade Técnica de Viena, especialmente ao Thomas Gebhard, à Barbara Weber e ao Alex.

Ao Carlos Parra e ao Zé Maria pelo trabalho teórico e pela amizade.

Aos professores e colegas do departamento de Física da UFMG, especialmente aos do grupo de Semicondutores.

Aos colegas e amigos da PUC-RJ e a todos os professores e alunos do DISSE.

À Marluce, Ieda, Shirley e todos os funcionários que colaboram para o bom funcionamento do departamento.

À Rachel pela amizade, apoio e carinho durante todas as fases do doutorado.

A todas as minhas amigas, amigos e familiares.

Foram 4 anos de dedicação. Ao longo desses anos várias pessoas contribuíram de alguma forma para a realização deste trabalho. Algumas, por motivos variados, não são mais presentes (ou são menos presentes) em minha vida. Agradeço a todos que contribuíram direta ou indiretamente para a realização desta Tese.

Ao CNPq, à CAPES, ao DISSE/INCT, ao Wolfgang Pauli Institute, pelo apoio financeiro.

"O único lugar onde sucesso vem antes do trabalho é no dicionário." Albert Einstein

RESUMO

Esta tese faz parte de uma proposta mais ampla cujo objetivo global é dominar a tecnologia de fotodetectores de radiação infravermelha baseados em pontos quânticos semicondutores auto-organizados, os *Quantum Dot Infrared Photodetectors* (QDIPs), para a faixa de comprimento de onda de 2 a 20 μm. A tese está centrada no estudo das propriedades físicas de pontos quânticos e de estruturas de QDIPs, em especial os mecanismos de transição intrabanda e de extração de carga envolvidos no processo de geração da fotocorrente. Foram estudadas estruturas inovadoras e originais baseadas em pontos quânticos auto organizados de InAs crescidos sobre substratos de InP. Para obter os principais resultados apresentados nesta tese foram feitas medidas de fotocorrente em função da temperatura e tensão externa aplicada, utilizando um espectrômetro de transformada de Fourier. As técnicas experimentais de fotoluminescência, microscopia de força atômica, microscopia eletrônica de transmissão e curvas de corrente *versus* voltagem também foram utilizadas para obter uma melhor compreensão dos mecanismos físicos envolvidos. Para explicar os resultados e atribuir cada pico de fotocorrente a uma transição específica utilizamos um modelo teórico tridimensional. Os resultados que se destacam e são apresentados nessa tese são:

i. O efeito Auger intrabanda é apontado como um possível processo importante para gerar a corrente nos QDIPs. Medidas de fotocorrente intrabanda e de absorção, juntamente com um cálculo teórico tri-dimensional, mostram que a transição responsável por gerar a fotocorrente medida em uma estrutura QDIP específica estudada ocorre entre estados ligados do ponto quântico onde o estado final da transição está 200 meV abaixo do contínuo. O espalhamento Auger é proposto como o mecanismo responsável pela extração de carga do ponto quântico, e portanto pela fotocorrente gerada, nesses dispositivos. Resultados de fotoluminescência e fotocorrente interbanda fornecem apoio adicional para esta conclusão.

ii. Diferentes estruturas nas vizinhanças do ponto quântico influenciam no sentido da corrente, pois os mecanismos de extração dos elétrons

dependem da estrutura como um todo. Os dispositivos aqui estudados apresentam fotocorrente com sentido positivo e negativo para a mesma tensão externa aplicada. Este duplo comportamento é atribuído à assimetria presente nessas estruturas, capaz de favorecer a extração de elétrons em um dos dois sentidos possíveis para a corrente. Esse processo foi observado apenas para pequenos valores de tensão externa aplicada. Para valores altos de tensão, os elétrons se propagam no mesmo sentido do campo elétrico aplicado, assim como esperado.

iii. Apresentamos um QDIP altamente seletivo com resposta espectral em torno de 12 μm. A estrutura estudada é composta por poços de InGaAs e pontos quânticos de InAs. A transição responsável pela fotocorrente observada ocorre entre estados ligados do ponto quântico, seguida por um mecanismo de extração de carga onde o acoplamento do estado final da transição com o poço de potencial vizinho ao ponto quântico tem um papel fundamental.

ABSTRACT

This thesis is part of a project where the overall goal is to master the technology of infrared photodetectors based on self-organized semiconductor quantum dots, the Quantum Dot Infrared Photodetectors (QDIPs) for the wavelength range from 2 to 20 μm. The thesis focuses on the physical properties of quantum dots and QDIPs structures, especially on the intraband transitions and extraction mechanisms involved in the photocurrent generation. We studied original and innovative structures based on self-organized InAs quantum dots grown on InP substrates. The main results presented in this thesis are based on photocurrent measurements as a function of temperature and external applied bias voltages, using a Fourier Transform Infrared spectrometer. The experimental techniques of photoluminescence, atomic force microscopy, transmission electron microscopy and current-voltage curves were also performed to achieve a better understanding of the physical mechanisms involved. To explain the results and assign each photocurrent peak to a particular transition, fully three dimensional theoretical calculations were done. The main results presented in this thesis are:

i- It is shown that the intraband Auger effect can be an important process for the photocurrent generation in QDIPs. Intraband photocurrent and absorption measurements, together with a full three-dimensional theoretical modeling revealed that a bound-to-bound optical transition, where the final state is about 200 meV deep below the conduction band continuum, is responsible for the photogenerated current in the particular QDIP structure investigated. Photoluminescence and interband photocurrent spectra further support this conclusion.

ii- We studied the influence of different structures in the neighborhood of the quantum dot on the photocurrent response of quantum dot infrared photodetectors. We measured a photocurrent with positive and a negative sign for the same external electric field in some QDIP structures. The dual sign photocurrent signal is attributed to asymmetries on the structures which can privilege the extraction of the carriers from the dots for

one of the two possible senses of the current. This process is seen for small external applied bias voltages or when no bias is applied. For high external fields the photoexcited electrons go in the same sense of the applied field, as expected.

iii- We present a very highly selective QDIP, which combines InAs quantum dots and InGaAs wells, operating at 12 μm. The transition responsible for the exceptionally narrow photocurrent is attributed to photon absorption between quantum dot bound states, followed by a carrier extraction mechanism where the coupling of the final state of the transition to the adjacent quantum well is highlighted

CONTENTS

RESUMO..v

ABSTRACT vii

1. INTRODUCTION...1

2. QUANTUM DOT STRUCTURES..4

2.1 Introduction to Quantum Dot Structures. 4

2.2 Quantum Dot Formation...5

2.3 Techniques for Material Deposition...7

2.3.1 Molecular Beam Epitaxy 7

2.3.2 Metal-Organic Vapour Phase Epitaxy...8

2.4 Experimental Studies on Quantum Dots Grown by MOCVD..........................9

References: 12

3. INFRARED DETECTORS 13

3.1 Infrared Technology 13

3.2 Infrared Photon Detectors...15

3.2.1 Figure of Merit 15

3.2.2 Types of Infrared Photon Detectors 18

3.3 Stand out works on Quantum Dots Infrared Photodetectors 21

3.4 How to Produce a QDIP 23

References 26

4. THEORETICAL MODELING...28

4.1 Introduction..28

4.2 Description of the Method 28

References 34

5. EXPERIMENTAL TECHINIQUES..35

5.1 Fourier Transform Infrared Spectroscopy 35

5.1.1 Sample Processing for Photocurrent Measurements 37

5.1.2 Sample Processing for Absorption Measurements........................... 39

5.2 Current-Voltage Measurements 40

References: 42

6. RESULTS 43

6.1 Introduction... 43

6.2 Evidences of Intraband Auger Process in Quantum Dot Infrared Photodetectors 44

6.3 Very Narrow Band QDIP Operating at 12 μm 54

6.4 Dual Sign Photocurrent in Quantum Dot Structures for Infrared Photodetection... 59

References 67

7. SUMMARY AND CONCLUSIONS 68

1. INTRODUCTION

The current technology of infrared (IR) detection is no longer fully attending the market needs. The rise of Information Technology and the Digital Economy require IR detectors with high sensitivity, high selectivity, high detectivity and low cost, small size and light weight. All of these requirements lead us to the development of new semiconductor technologies and materials.

With the advances in epitaxial growth of heterostructures a new class of material with unique optoelectronic properties has been developed. This new concept consists on zero dimensional quantum confined semiconductors heterostructures, called Quantum Dots (QDs), with several promising applications like more selective detectors, lasers, solar cells, and others. Researchers have studied the application of QDs in solar cells, LEDs (light emitting diodes), optical communication in free space, etc, apart from the wide application in imaging (including medical image). QDs have also been suggested as implementation of quibts for quantum information.

Much attention has been devoted to these heterostructures for mid-infrared photodetection applications. The interest on this zero dimensional structures is due to their potential for the development of selective infrared detectors operating close to, or even, at room temperatures, with high detectivity.

Theoretical predictions show that quantum dots infrared photodetectors (QDIPs) can out-perform direct band gap Detectors, which are commonly called MCT detectors from Mercury Cadmium Telluride, and quantum well infrared photodetectors (QWIPs), which dominate the IR detector market nowadays. In the case of direct band gap detectors, the mechanism that generates the detection is a band to band transition (valence band-conduction band), which make these detectors very efficient devices. On the other hand they are not selective devices. The major disadvantage of MCT is that due to a dramatic change of the band gap as a function of material composition it is very challenging to obtain large area homogeneous materials suitable for Focal Plane Arrays (FPAs). In addition, this alloy material is difficult to work with, being very brittle. In contrast, QWIPs are generally made of III-V materials, and benefit from a well developed technology. In QWIPs the transition generated by the absorption of the

radiation is intraband. It occurs in the conduction band (or in the valence band) between a bound quantum well state and a state in the continuum (or close to the continuum). This makes QWIPs more selective devices when compared to MCTs detectors. The main drawback of QWIPs is the presence of selection rules which forbid the absorption of normal incident light. The result is that QWIPs are not very efficient and they demand the use of diffraction gratings on top of the device or some other artifact to change the direction of normal incident radiation. Besides that, QWIPs only work at low temperatures due to a high dark current generated by the large density of states in quantum well structures when compared to quantum dot structures. In QDIPs the transitions involved in the detection are also intraband. As the QD confine the electron in all three dimensions the selection rules are no longer a problem in these structures. Also, since the energy levels are discrete, and not subbands as in QWIPs, the QDIPs are even more selective. Besides that, the longer life time of the carriers in these structures increases the detectivity.

The biggest problems faced by QDIPs nowadays are related to the difficult in controlling the QD size, density and homogeneity. These QD parameters are directly related to IR detector properties. For example, the QD size is one of the parameters that set the detection wavelength and the QD density and uniformity influence the detectivity.

In this thesis we present a study on new structures and materials for IR photodetection. We designed structures based on self-assembled InAs QDs grown by Metalorganic Chemical Vapor Deposition (MOCVD) on InP substrates. Nowadays there are only a few studies on the InAs/InP system for QDIPs. The most studied material system for the development of QDIPs is InAs/GaAs quantum dots. Although being formed by the same quantum dot material, the two systems differ in important points, which generate differences in the optical and electronic properties of the device. The most important difference is related to the lattice mismatch that is smaller for InAs/InP systems.

In Chapter 2 we present some important concepts of QDs. Chapter 3 is dedicated to IR photodetectors. In Chapter 4 we talk about the theoretical modeling used to calculate the electronic structure of the devices. In Chapter 5 we explain the experimental procedure and in Chapter 6 we show the most important results of this work, which are focused on the physical properties of quantum dots and QDIPs

structures, especially on the carrier extraction mechanisms. We show the importance of intraband Auger processes to generate a photocurrent. We study the influence of the final state of the transition on the carrier extraction mechanisms. We present a very selective QDIP structure which operates at around 12 µm. The final chapter is devoted to the main conclusions.

Enjoy the reading!

2. QUANTUM DOT STRUCTURES

2.1 Introduction to Quantum Dot Structures.

When we talk about Quantum Dots (QDs) we are talking about quantum confinement, which affects crucially the properties of particles and systems. A QD is the ultimate limit of confinement for carriers, since the particles are constrained in all 3 directions. This means that the electrons (and/or holes or excitons) are localized in space. As a consequence, the energy states allowed for the carriers are discrete, as in atoms [2.1].

In a bulk material the density of states, which describes the number of states per energy that are available to be occupied is a continuous function of the band energy. In a 2-D structure, like a Quantum Well (QW), the electron is now constrained in one direction but free to move along the plane, which results in a density of states that increases with energy in steps (Figure 2.1). If now we confine the electrons in a second direction, there remains free motion only in one direction. These structures are called quantum wires. And if the electrons are confined in all 3 directions, then we have discrete states as the electron is not free to move and only certain energy states are allowed, as shown in Fig. 2.1 [2.1, 2.2]. Due to this characteristic the QDs are sometimes called artificial atoms.

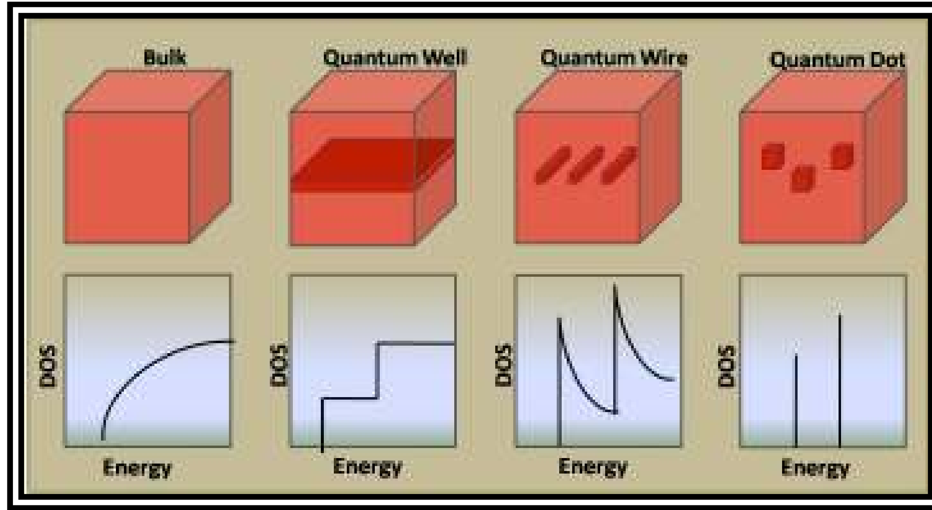

Figure 2.1: Schematic plot of the Density of States (DOS) as a function of the energy for systems of different dimensionalities.

2.2 Quantum Dot Formation

There exist several different methods to form a QD [2.3]. In this thesis it is explained the most common method to form a QD for Infrared Photodetectors (QDIPs), called Stranski- Krastanow [2.3-2.6] growth mode.

Consider a system that consists of two different materials, A and B. Suppose material A is deposited on material B and that these two materials have different lattice constants. If they have the same crystal structure and slightly different lattice constants (difference of less than 1%), then material A will assume material's B lattice constant and a coherent deposition will happen. A second possibility would be the case that the lattice constant of material A is somewhat larger (of the order of a few percent difference) than that of material B. In this case a phenomenon called Stranski-Krastanow growth could be observed. In the first deposited layers, material A assumes the lattice parameter of material B. This gives rise to an elastic energy that gets higher and higher as more material is deposited. After a certain thickness this elastic energy can no longer be supported and the system relaxes, to minimize the energy, and 3D islands called Quantum Dots are formed. These nanostructures form spontaneously and can also be grown coherently, the latter property depending on the thickness between the layers. When this is the case, the material A islands formed are called self-

assembled quantum dots. The couple of layers or so with the same lattice constant of material B is denominated wetting layer (Figure 2.2). To form Stranski-Krastanow QDs a slow deposition is required, in the order of 100 nanometers per hour. The most common techniques used nowadays for this kind of QD formation are Molecular Beam Epitaxy [2.1, 2.2, 2.3, 2.7, 2.8], MBE, and Metal-Organic Chemical Vapor Deposition [2.1, 2.2, 2.3, 2.9], MOCVD, briefly described in the following sections.

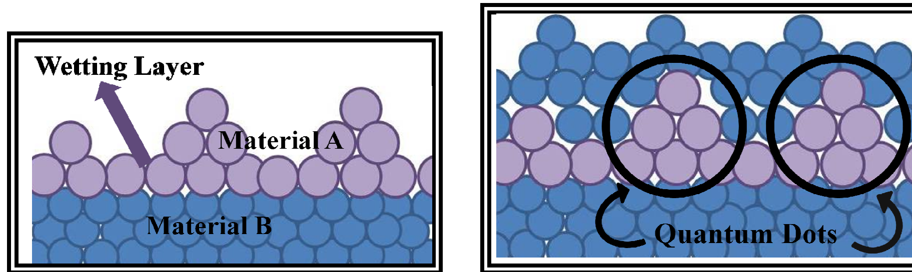

Figure 2.2: Deposition of material A over material B, for materials with different lattice constants. The first layer of material A is coherent and is called wetting layer. After a certain critical thickness quantum dots are formed. In the right hand side, the QD are then covered with material B.

In the other cases, like when the lattice parameter of material A is smaller than material B, than different types of dislocations will occur. This was studied by van der Merwe in 1949 [2.2, 2.10].

It is important to notice that in order to obtain good quality thin films and QDs, the materials A and B should be similar. They should have equal or similar crystal structures, the same valences (III-V semiconductors are easier to grow on III-V, and so on). The lattice mismatch is also a crucial point in an epitaxial growth. Figure 2.3 [2.1] shows a diagram of the band gap energy as a function of the lattice constant for the most important semiconductors alloys for this thesis.

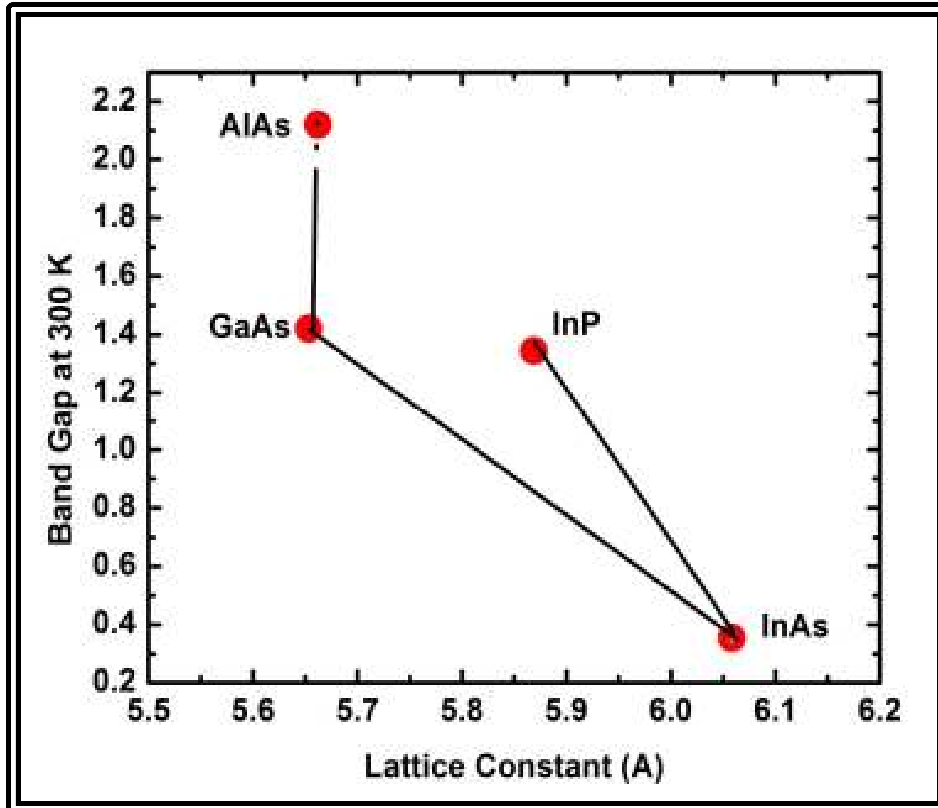

Figure 2.3: Band gap energy as a function of the lattice constant for the semiconductor systems studied in this thesis [based on Figure 8.31 from ref.2.1].

2.3 Techniques for Material Deposition

The two most important techniques to deposit materials layer by layer to produce thin films are 1) Molecular Beam Epitaxy (MBE) [2.1,2.2,2.3,2.7,2.8] and 2) Metal-Organic Chemical Vapour Deposition (MOCVD) also known as Metal-Organic Vapour Phase Epitaxy (MOVPE) [2.1,2.2,2.3,2.9].

2.3.1 Molecular Beam Epitaxy

The growth takes place in a chamber in ultra high vacuum (Figure 2.4). Pure elements like gallium, arsenic, and indium are heated in separated cells (effusion cells) until they begin to evaporate or sublimate. The cells with very small orifices are positioned pointing to the substrate which is placed in the middle of the chamber. By opening the shutters it is possible to grow thin films.

The biggest advantages of MBE growth are the good quality of the interface materials and the possibility to control the quality of the deposited materials *in-situ*, during growth. The most commonly used techniques for this purpose are Reflection High Energy Electron Diffraction (RHEED) and Mass Spectroscopy [refs]. Some other techniques like Auger Electron Spectroscopy (AES) and Low Energy-Electron Diffraction (LEED) are also used [2.1-2.3]. These techniques can be used to obtain *in-situ* control because the growth chamber is in Ultra-High Vacuum. The disadvantage of the MBE is the high cost..

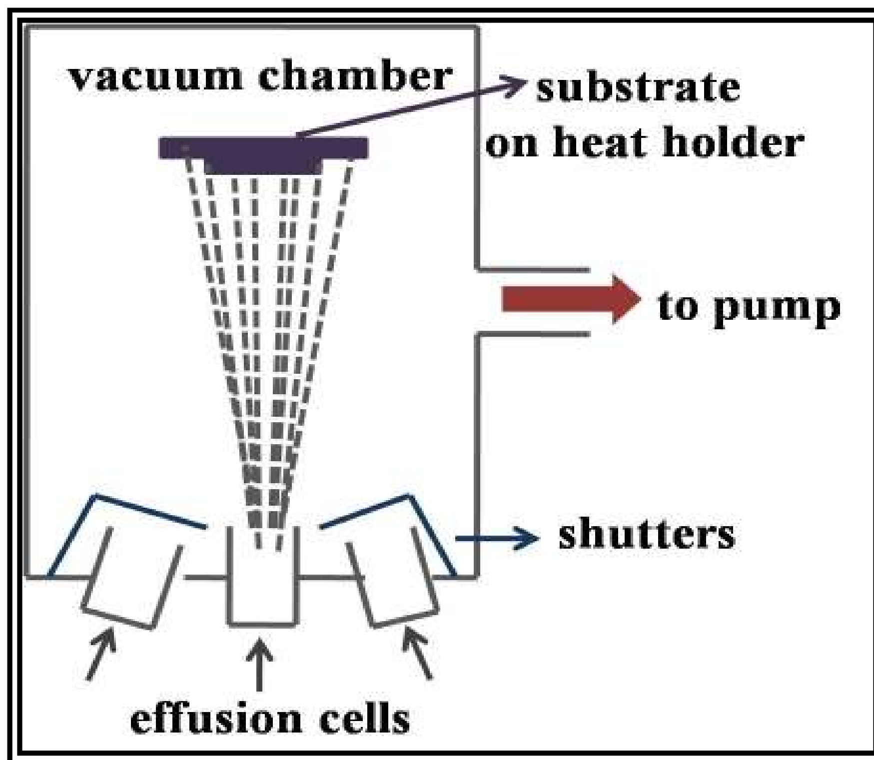

Figure 2.4: Schematic picture of a MBE system. The growth takes place inside a vacuum chamber. Pure elements inside the cells pointed to the substrate are heated until sublimation. (based on Figure 8.30 from ref 2.1).

2.3.2 Metal-Organic Vapour Phase Epitaxy

In MOVPE the growth takes place inside a reactor at relatively high pressure. A schematic picture of the reactor is presented in Figure 2.5. The growth rate is controlled by controlling the amount of gas flow. The thin layer is formed by a reaction of the gases containing the required chemical elements that will be deposited. To deposit

silicon (Si), the gas used is SiH_4 which breaks in Si + $2H_2$. The Si remains on the substrate and the H_2 is collected in the exhaust. The other common gases used in MOVPE are PH_3, AsH_3, $Ga(CH_3)_3$. To grow a GaAs thin film, the chemical reaction is $Ga(CH_3)_3$ + AsH_3 producing $3CH_4$ +GaAs. The disadvantage of this technique is the need of highly toxic gases and the bad quality interfaces.

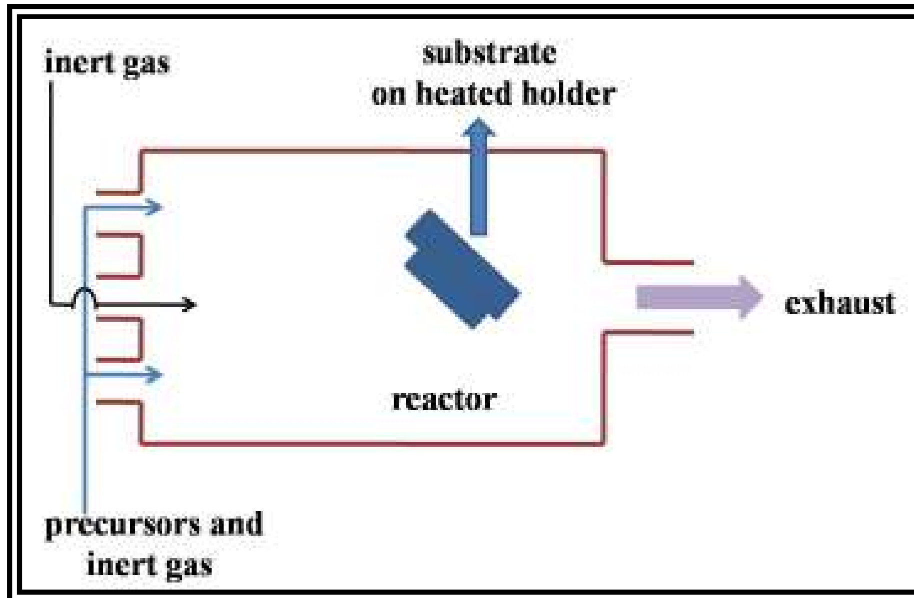

Figure 2.5: Schematic drawing of a MOVPE system. The growth takes place inside a reactor. Film deposition occurs after a chemical reaction. An inert gas is used to control the flux. (based on Figure 8.30 from ref 2.1).

2.4 Experimental Studies on Quantum Dots Grown by MOCVD

In this thesis we study quantum dot structures to produce photodetectors in the infrared region. According to theoretical predictions, these structures have the potential for the implementation of selective devices with high detectivity due to the 3D confinement of carriers. It is believed that one of the main reasons that prevent achieving these predictions is related to the lack of control of the quantum dots growth. As it is a process of spontaneous formation, it ends up generating a broad size distribution of quantum dots. Besides that, the control of the density and spatial distribution of the dots is still a problem faced by the growers. Due to this, studies on quantum dot formation were developed by several groups.

Borgstrom *et al.* [2.11] studied InAs QDs prepared on an InAlGaAs surface by metal organic vapor phase epitaxy. Figure 2.9a-c shows Atomic Force Microscopy (AFM) images and the corresponding height, obtained from these images of InAs QDs on $In_xAl_yGa_{1-x-y}As$, with increasing Al content from (a) to (c). This study demonstrates that dots grown on material with higher Al content are smaller and that the dot density is increased. PL measurements show (Figure 2.10) that these dots luminesce at 2.1 µm and that the emission is blue shifted when the Al content is increased.

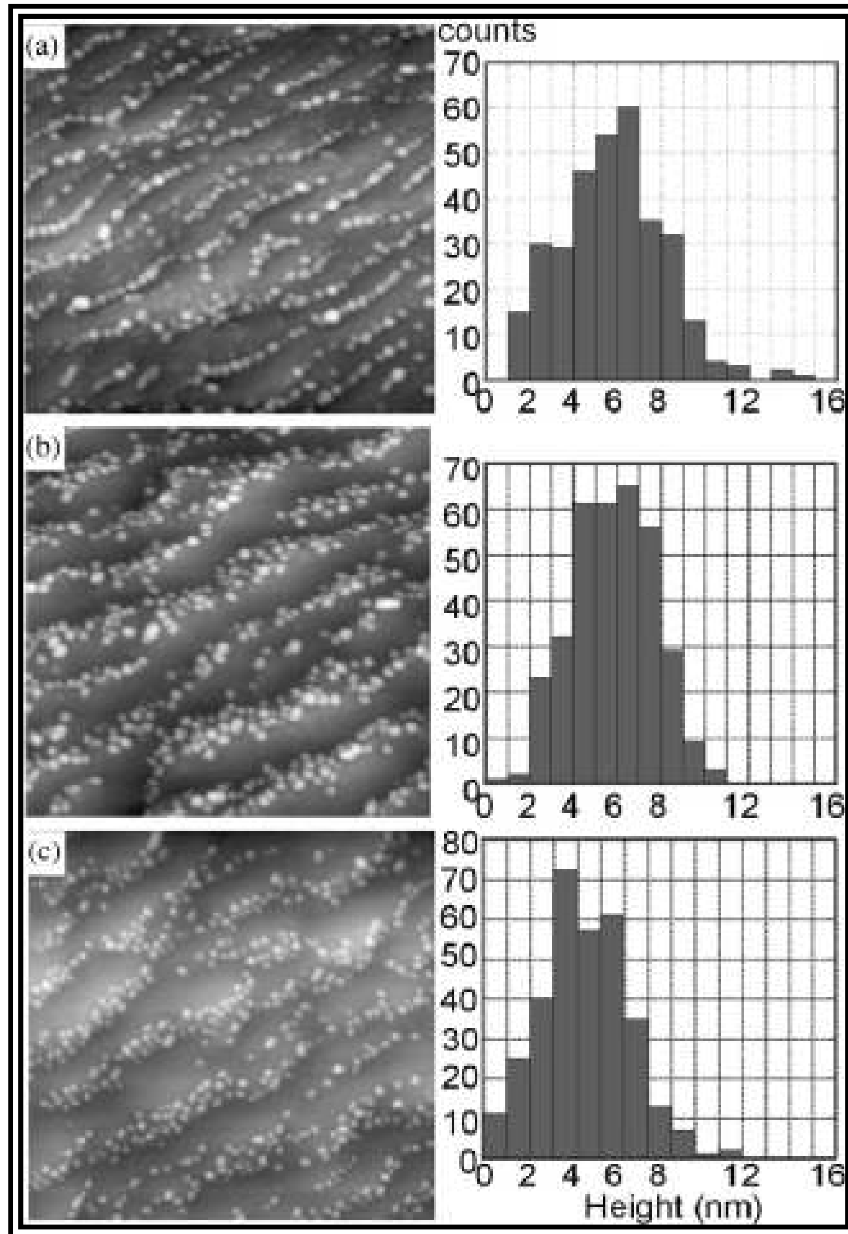

Figure 2.9: 2 x 2 µm^2 AFM images and corresponding dot height on $In_xAl_yGa_{1-x-y}As$ with (a) y = 0; (b) y = 0.11; (c) y = 0.16 [2.11].

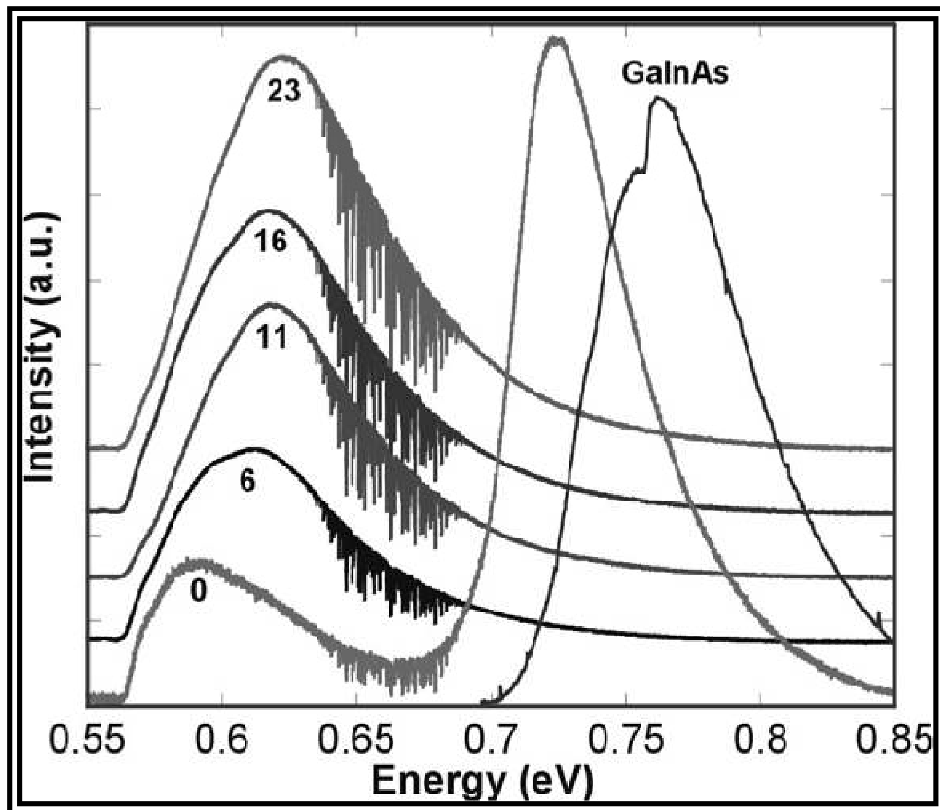

Figure 2.10: PL spectra for InAs/ $In_xAl_yGa_{1-x-y}As$ QDs samples. The numbers represent the percentual Al concentration [2.11].

References:

[2.1] C. Klingshirn, *Semiconductor Optics*, 3rd Edition, Springer.

[2.2] P. Yu, M. Cardona, *Fundamentals of Semiconductors: Physics and Materials Properties.* 3rd Edition, Springer.

[2.3] D. Bimberg, M. Grundmann, N. Ledentsov, *Quantum dot heterostructures,* Wiley.

[2.4] I.N. Stranski, L. Krastanow, *Sitzungsber Akad. Wiss. Wien Math, Naturwiss,* K1 Abt. 2B Chemie **146,** 797 (1937).

[2.5] D.J. Eaglesham, M. Cerullo, *Physical Review Letters* **64**, 1943–1946 (1990).

[2.6] C. H. Chiu, Z. Huang, C.T. Poh, *Physical Review Letters* **93**, 136105 (2004).

[2.7] L.Goldstein, F.Glas, J. Y. Marzin, M. N. Charasse, G. Le Roux, *Applied Physics Letters* **47**, 1099 (1985).

[2.8] R. J.Warburton, *Contemporary Physics* **43**, 351 (2002).

[2.9] M.Razeghi, *The MOCVD Challenge*: *A survey of GaInAsP-InP and GaInAsP-GaAs for photonic and electronic device applications*. Second Edition. Taylor and Francis/CRC Press, 2010.

[2.10] F. C. Frank, J.H. Van Der Merwe, *Proceedings of the Royal Society A* **198**, 216-225 (1949).

[2.11] M.Borgstrom, *Journal of Crystal Growth* **252**, 481–485 (2003).

3. INFRARED DETECTORS

3.1 Infrared Technology

The infrared region is a large region of the electromagnetic spectrum that goes from 0.740 microns (end of visible spectra-red) until around 1000 microns, where microwaves start. In Figure 3.1 the entire spectrum is presented schematically with the divisions and subdivisions. According to the International Organization of Standardization, ISO 20473, the infrared band is subdivided in near infrared, mid infrared and far infrared as in Figure 3.1. When we talk about sensors, the infrared spectra are subdivided according to the response of various detectors. The near infrared goes from 0.74 to 1.0 micrometers (from the end of the response of the human eye to the response of silicon). The short-wave infrared goes from 1.0 to 3 µm (from the cut off of a silicon detector to the MWIR atmospheric window, a InGaAs-based detector covers up to about 1.8 micrometers). The mid-wave infrared comprises the wavelengths from 3 to 5 micrometers (defined by the atmospheric window and covered by detectors based on indium antimonide – InSb – and the HgCdTe alloy and partially by lead selenide – PbSe). The long-wave infrared goes from 7 to 14 µm (HgCdTe detectors and microbolometers) and very-long wave infrared is from 12 to about 30 µm, covered by doped silicon detectors.

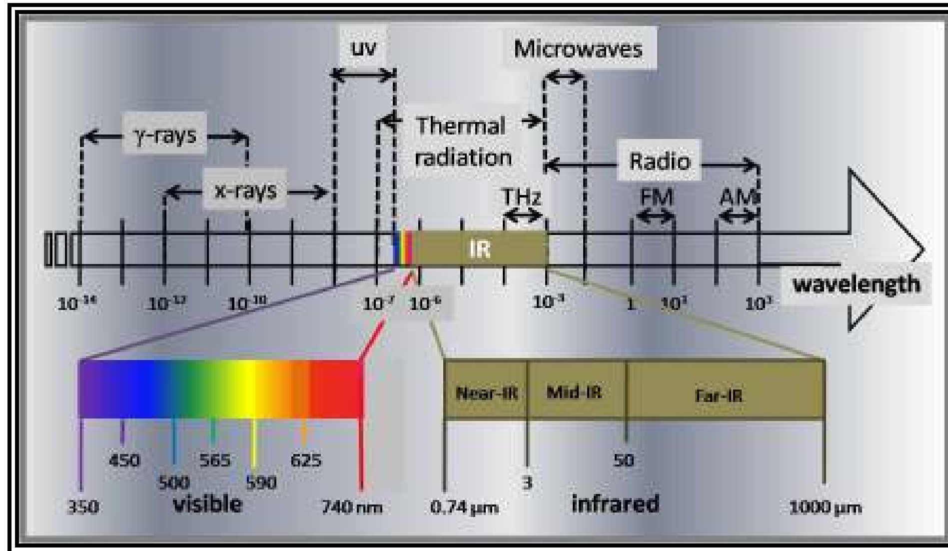

Figure 3.1: Part of the electromagnetic spectra in wavelength.

Initially, the interest in the IR region was mainly due to thermal radiation and the development of IR detectors was connected to thermal detectors [3.1, 3.2], but they are limited in sensitivity and range. Around 1860, for the first time, the IR radiation from the moon, planets and bright stars could be detected. It was only 100 years later that the IR detector technology was advanced enough to allow mapping the sky and more than 20000 IR sources were then discovered (all of them stars that could not be seen with the naked eye) [3.2].

The history of IR is reviewed in Barr's [3.3] paper and two well-known monographs [3.4, 3.5] and in the past few decades, the IR region was intensively studied due to a wide variety of applications [3.6-3.10].

The IR detectors are subdivided in thermal detectors and photon detectors and the difference between then are the detection mechanism: in thermal detectors the absorption of the incident light results in a change of the temperature of the detector and consequently in resistance, and in photon detectors the mechanism is based on photoexcitation. This thesis is focused on quantum dot infrared photodetectors and the detection mechanism is based on photoexcitation.

Infrared devices can be used for gas detection, remote sensing, optical communications in free space, etc [3.8-3.12]. In addition to that, there is a remarkable amount of applications in imaging. In medicine, for example, with a simple infrared

image it is possible to identify and locate a health problem [3.9-3.10]. When a region of the human body is inflamed, the temperature changes and can be detected by the difference in the amount of radiation it emits, relative to a healthy area of the body. Following this line of reasoning we find several other applications in medicine, like as monitoring the healing after surgery or for the early detection of skin cancer. Still in the imaging field, we can mention applications in the industrial area to determine the level of a liquid in a tank, or even to locate obstructions in pipes. Another application that has attracted much attention recently is systems of imaging infrared heat to aid the pilots of aircraft on approach for landing.

But, mainly, IR technology was and continues to be driven by military applications [3.2]. Due to this, the technology of infrared sensors and systems is highly protected by the countries that dominate it and the purchase by Brazil of devices or sensitive equipment in that band of the electromagnetic spectrum is often difficult or even not allowed. That is why Brazil should develop its own technology for infrared detection and this involves a detailed study of semiconductor structures.

3.2 Infrared Photon Detectors

3.2.1 Figure of Merit

There exist different types of IR photon detectors, which will be discussed in section 3.2.2. Due to the variety of IR detector, a few parameters are defined to make possible the comparison of the performance of these devices and, of course, to make a quantitative characterization of different detectors. Here, we focus on photoconductive photon detectors, where the detection mechanism is based on photoexcitation. The incident radiation excites an electron to the continuum of energy levels in the conduction band, this electron drifts towards the collector and a photocurrent is created.

The first parameter to be defined is the responsivity,R_i, which measures the generated photocurrent I_{out} per incident optical power P_{in} (ratio of output and input), given in units of A/W of the incident radiation power [3.1, 3.2, 3.13]. It is defined as:

$$R_i = \frac{I_{out}}{P_{in}} = \eta g \frac{q}{h\nu} \ , \tag{3.1}$$

where q is the elementary charge, $h\nu$ is the photon energy absorbed with an efficiency η and g is the gain (Figure 3.2). The gain is the capacity of the detector to increase the output signal from the input. It is defined as:

$$g = \frac{\tau_{life}}{\tau_{tran}} \ , \tag{3.2}$$

where τ_{life} is the carrier lifetime and τ_{tran} is the carrier transit time. From this equation one can conclude the importance of both quantities. The carrier lifetime is the average time that the carrier takes to recombine. The transit time is the time that the electron needs to cross the active region and it is larger for thicker samples.

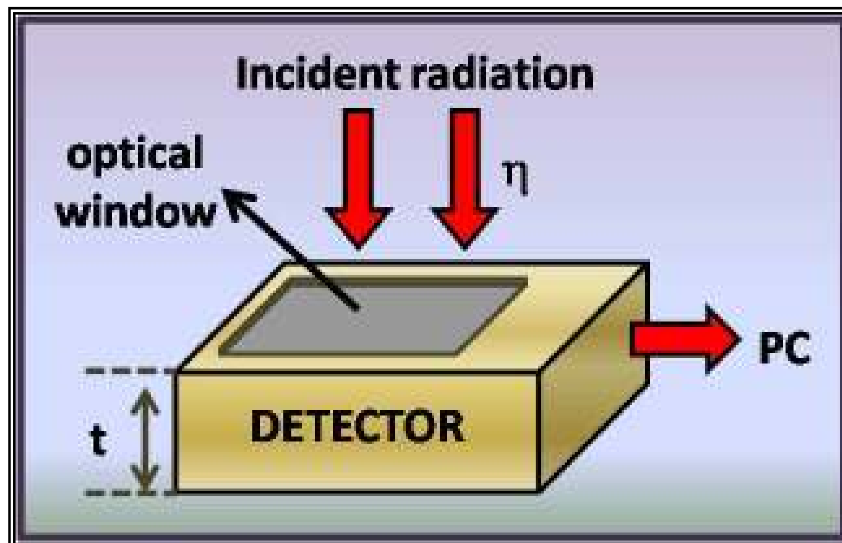

Figure 3.2: Scheme of a QDIP of thickness t. The incident radiation is absorbed with efficiency η and generates a photocurrent PC.

The responsivity is an important parameter, but, alone is not enough to characterize a detector, as it does not say anything about the sensitivity which is the minimum detectable signal.

The sensitivity can be quantified by measuring the noise i_{noise}. In the case that the noise bandwidth is as large as the generated signal, it would be impossible to discriminate both. Different mechanisms can contribute to the noise [3.1, 3.2], like temperature noise, photon noise, generation-recombination noise I_{GR} and others. In the case of Quantum dots Infrared Photodetectors, the last one is the dominant noise mechanism [3.14] and can be estimated by measuring the dark current I_D.

The I_{GR} is a result of the generation-recombination rates of the electrons between different energy states of the material. It is a statistical process that depends on too many parameters and is very difficult to calculate. The dark current I_D is the current that flows without input signal. This current can be generated by mechanisms like thermionic emission, thermal assisted tunneling and sequential tunneling. These mechanisms depend on the structure and on the bias and temperature of operation.

The relation between the dark current and the generation-recombination noise is given by:

$$I_{GR}^2 = 4eg\Delta f I_D \tag{3.3}$$

where is e electron charge, g is the gain and Δf is noise bandwidth.

Actually, the figure of merit of a photodetector which is more important is the so-called detectivity D, which is a quantitative value for the signal to noise ratio of the device at a given bias and temperature, for a specific wavelength [3.13 - 3.16]. In the literature it is referred as the inverse of a quantity defined as noise equivalent power P_{NEP}.

$$D = \frac{1}{P_{NEP}} = \frac{R_i}{i_{noise}} \tag{3.4}$$

The specific detectivity D^* is then defined as the detectivity of a photodetector with an area of 1 cm^2 and an electrical bandwidth of 1 Hz.

$$D^* = \frac{R_i}{i_{noise}} \cdot \sqrt{A.\Delta f} \ , \tag{3.5}$$

where Δf is the bandwidth and $A$is the detector area. The unit for D^* is the *Jones* (cm x Hz ^{½} /W) in honor to R. Clark Jones who defined this magnitude [3.15, 3.16].

3.2.2 Types of Infrared Photon Detectors

According to Martyniuk [3.17] the majority of infrared photon detectors in use nowadays can be divided into five classes:

i) direct band gap semiconductors (InSb, InAs, HgCdTe or MCTs, etc),
ii) extrinsic semiconductors (Si:As, Ge:Hg, etc),
iii) superlattice (GaAs/AlGaAs QWIPs),
iv) Silicon Schottky barrier (PtSi, IrSi) and
v) quantum dots (InAs/GaAs, InAs/InP,etc).

The most common photodetectors for the IR region used nowadays are direct band gap semiconductors (especially MCTs) [3.18-3.20] and type-I superlattice (QWIPs). [3.21,3.22]. In the case of MCT detectors, the mechanism that generates the detection is an interband transition (valence band-conduction band), which make MCTs very efficient devices. On the other hand they are not selective devices. Another big advantage of MCTs is that, by varying the cadmium and tellurium concentrations in the alloy, moving from HgTe to CdTe, it is possible to change the gap energy from 0 to 1.44 eV, without much change in the lattice parameter. Figure 3.3 shows the gap energy as a function of lattice parameter for different materials.

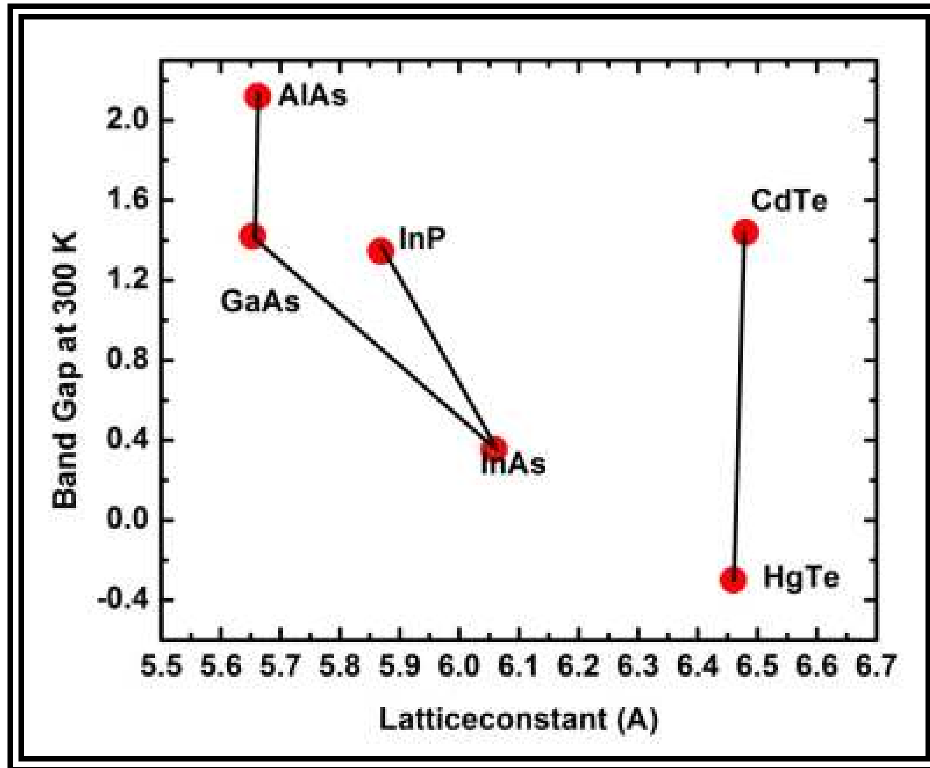

Figure 3.3: Band gap energy and lattice constant for important material for infrared photodetectors

In general, in QWIPs the transition generated by the absorption of the radiation is intraband. It occurs in the conduction band between a bound quantum well state and a state in the continuum. This makes QWIPs more selective devices when compared to MCTs detectors. The drawback of QWIPs is the presence of selection rules which forbid the absorption of normal incident light. This makes QWIPs not as efficient and they demand the use of diffraction gratings on the top of the device or some other artifact to change the direction of normal incident radiation. Besides that, QWIPs only work at low temperatures.

Recently, it was proposed the development of infrared photodetectors based on self assembled quantum dots, called quantum dot infrared photodetectors (QDIPs) [3.23,3.24]. The first QDIP was demonstrated in 1998 [3.25]. In QDIPs the transitions involved in the detection are also intraband. As the QD confines the electrons in all three dimensions the selection rules are no longer a problem in these structures. Besides that, the longer lifetime of the carriers in this structures increase the detectivity [3.26],

as showed in sub-section 3.2.1 of this thesis. Finally, the dark current in QDIPs is expected to be lower [3.27].

Since the proposal of these new structures, a lot of attention has been devoted to them [3.28-3.34]. The intense study on self assembled quantum dots is in part due to their potential to suppress other material systems for infrared photodetection. Figure 3.4 presents a graph [3.17] of the calculated detectivity, for different types of photodetectors operating at 5 μm and in Figure 3.5 the predicted detectivity for photodetectors operating at 10 μm [3.17]. The assumed quantum efficiencies are indicated in the figures. Theoretical estimations for QDIPs are carried out assuming low quantum efficiency of 2% (often measured in practice) and high efficiency of 67%. The last value is typical for HgCdTe photodetectors. From this graph we can conclude that the detectivity of high efficiency QDIPs are comparable to the performance of HgCdTe photodetectors. We can also notice that AlGaAs/GaAs QWIPs have better performance than extrinsic silicon photodetectors.

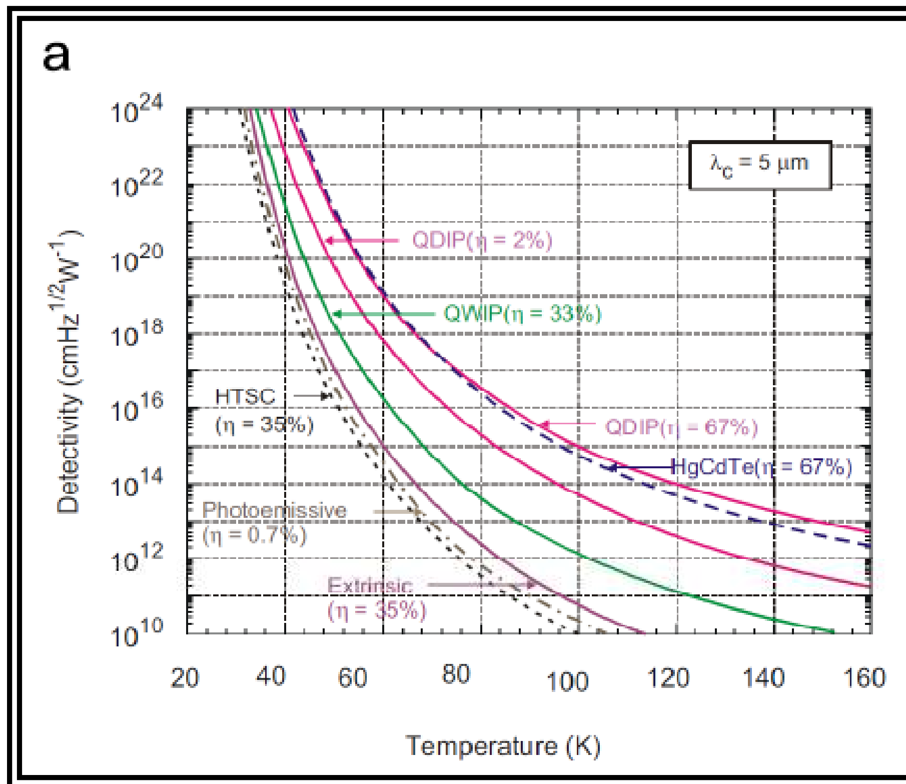

Figure 3.4: Predicted detectivity as a function of temperature for different photodetectors operating at 5 μm [3.17].

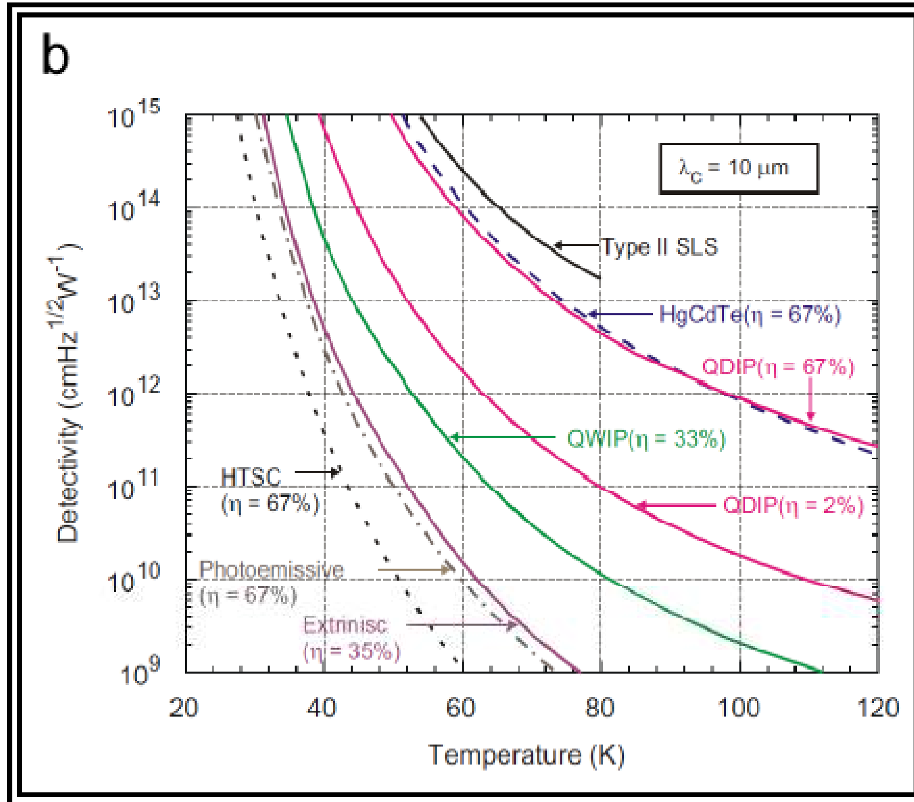

Figure 3.5: Predicted detectivity as function of temperature for different types of photodetectors operating at 10 μm [3.17].

3.3 Stand out works on Quantum Dots Infrared Photodetectors

The most studied system in the literature for infrared photodetection applications are InAs/GaAs. In this thesis I report results on the InAs/InP QD based system. Even though they have the same quantum dot material, they differ in three important aspects, which lead to different electronic and optical properties of the two systems [3.35]:

i- InAs/InP has much smaller lattice mismatch (3%) when compared to InAs/GaAs (7%) (See picture in section 1.3);

ii- InAs/InP has a weaker confining potential for electrons, but stronger for holes;

iii- InAs/InP dots share the same cation (In), while in InAs/GaAs the anion (As) is the same.

In addition to new materials, new concepts and innovative structures also need to be investigated. An interesting proposal, presented in 2006 to increase the efficiency of photodetectors based on intraband transitions, is the so-called Tunneling Quantum Dot Infrared Photodetector (T-QDIP) [3.33]. Double AlGaAs/InGaAs barriers are inserted, generating resonant levels and blocking the dark current. The transport of carriers is done by tunneling. Figure 3.6 shows the potential profile of the structure studied by Bhattacharya *et al.* [3.33]. This structure, grown on a GaAs substrate, has a spectral response around two frequencies (6 μm and 17 μm) and has obtained good results for detectivity at room temperature for 17 μm.

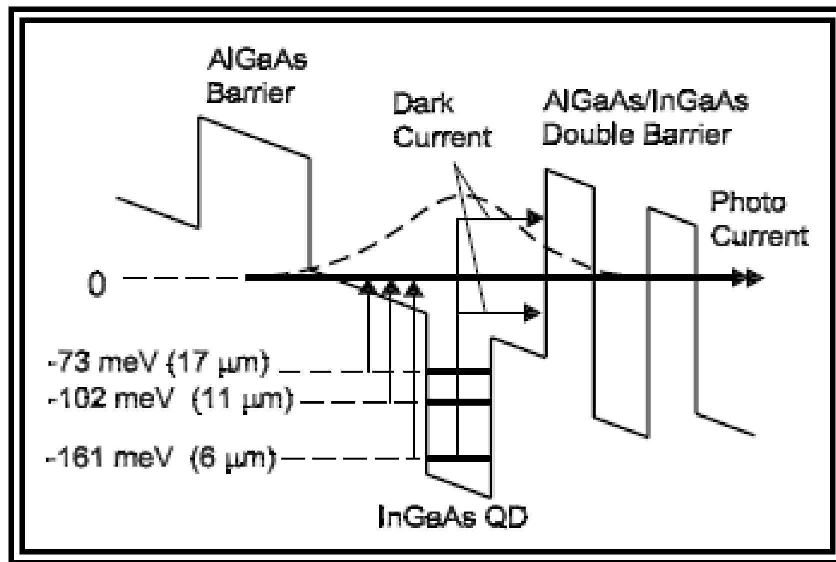

Figure 3.6: Conduction band diagram of a Tunneling QDIP structure [3.33] and the calculated energy levels. The electrons that are not at the resonant level are blocked by the barrier.

In these T-QDIP structures the tunneling probability for the excited carriers in the resonant level is near unit while all the other carriers are blocked by the barrier. In this sense it is possible to introduce a high potential barrier for the thermal excitations with lower photo excitation energy. As a result, the operating temperature can be significantly increased.

Little study has been performed on devices based on InP substrates, and these have shown more promising results than the most studied InAs/GaAs QD system. In 2007, Lim *et al.* [3.28] presented a quantum dot structure inserted in a quantum well,

dots in the well, D-WELL, with high responsivity and low dark current. Some photocurrent results are shown in Figure 3.7.

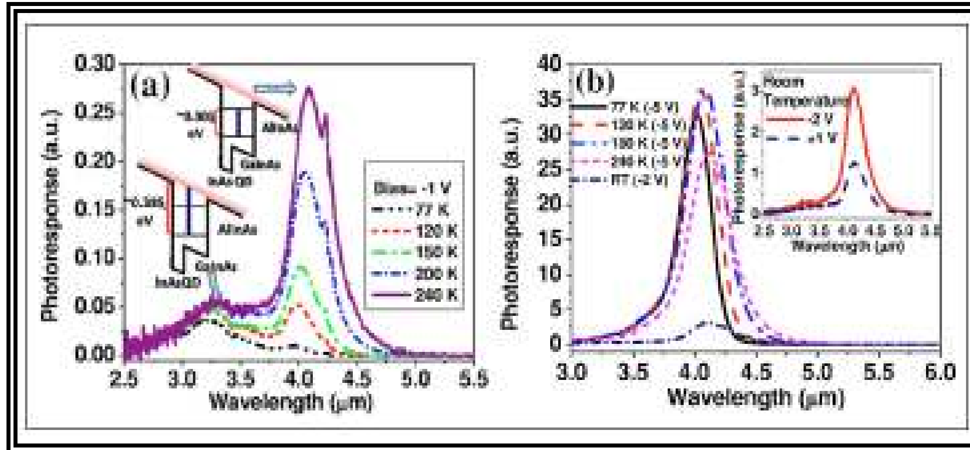

Figure 3.7: Photocurrent results obtained by Lim et al. for D-WELL samples. In (a) is presented the photocurrent as function of temperature, measured at a bias voltage V = -1 V. In (b) he shows the photocurrent response for V = - 5 V and V = - 2 Vas function of temperature. In the inset is presented the results at room temperature measured with V=-2V and V=+1 V.

Greater understanding of the involved mechanisms in intraband transitions of QD structures is required for planning more efficient devices. Despite the intense effort in the last two decades, the physics of self-assembled quantum dot structures for mid-infrared photodetection implementation has several unanswered questions.

3.4 How to Produce a QDIP

The fabrication of a QDIP is complicated and involves delicate procedures that demand knowledge and time. The scheme of a QDIP structure is presented in Figure 3.5.

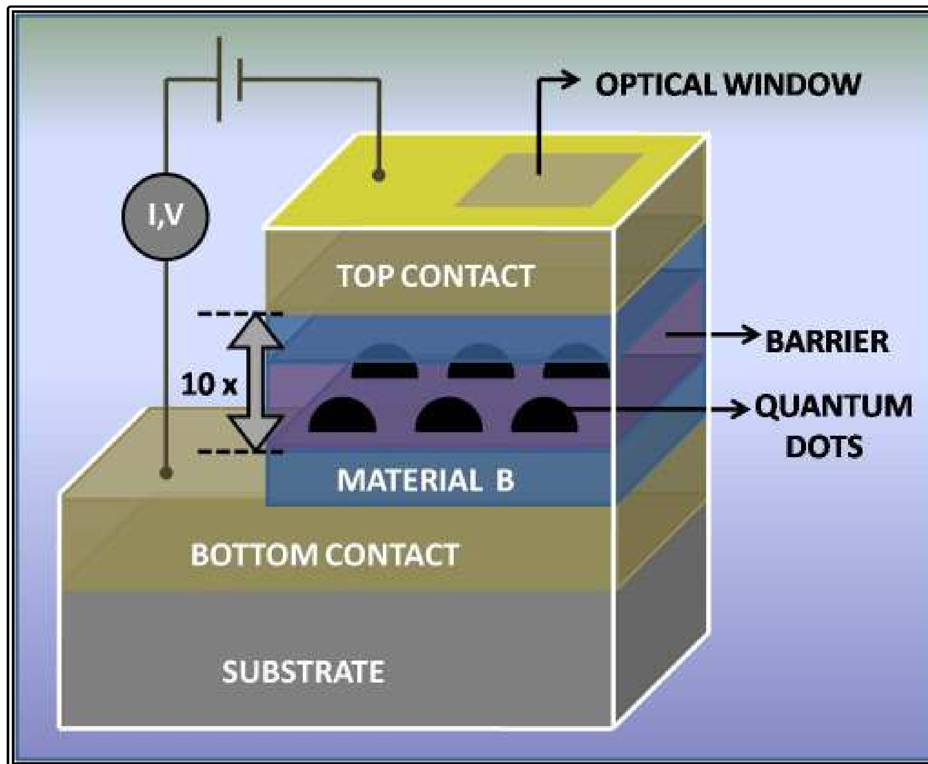

Figure 3.5: Quantum dot infrared photodetector scheme.

The procedure starts by the definition of all the parameters of the structure, which depends on the kind of detector we want to produce. The structure influences the spectral response of the detector, not only the wavelength of the detection but also the type of detector, narrow or broad band. The material of the structure also influences the response of the device, since different materials have different band offsets and different optical properties. The thickness and height of the barrier also affect the detection wavelength and the magnitude of the dark current.

Excluding the setting of the structure parameters, we could divide the process into two parts. The first one consists of the sample growth and characterization, and the second part is the device fabrication and characterization.

As said in the previous Chapter the most common techniques to grow a quantum dot structure to produce a QDIP are MOVPE and MBE. The samples studied in this thesis were grown by MOVPE by Maurício Pamplona Pires and Patrícia Lustoza Souza at PUC-Rio.. The size of the quantum dot is also an important parameter as it strongly

influences the detection wavelength. In the case of intraband bound-to-continuum transitions, for larger dots the ground state is lower in energy, which gives a shorter operation wavelength. The density and uniformity of the dots affect the detectivity of the device. The higher these latter parameters are, the higher is the responsivity. The doping of the dots also has an effect on the responsivity and dark current.

To characterize the QD samples several techniques like Atomic Force Microscopy - AFM, Transmission Electron Microscopy TEM, absorption and photoluminescence - PL are generally used. The samples studied here were analyzed by all these four techniques. For AFM measurements, samples with uncapped dots were prepared. For the absorption measurements, we grew samples with 20 periods and without contact layers.

The device fabrication and characterization consist on processing the sample in a device form (detailed in section 5.1.1). The characterization and study of the devices was mainly done with photocurrent and IV measurements. These two techniques allow us to determine the spectral response of the device and to calculate the detectivity.

References

[3.1] M.A. Kinch, *Jornal of Electronic Materials* **29**, 6 (2000).

[3.2] A. Rogalski, J. Antonszewski, L. Faraone, *Jornal of Applied Physics* **105**, 091101 (2009).

[3.3] E. S. Barr, *American Journal of Physics* **28**, 42 (1960).

[3.4] R. A. Smith, F. E. Jones, R. P. Chasmar, *The Detection and Measurement of Infrared Radiation.* Clarendon. Oxford, (1958).

[3.5] P.W. Kruse, L.D. McGlauchlin, R.B. McQuistan, *Elements of Infrared Technology.* Wiley. New York , (1962).

[3.6] P. Norton, J. Campbell, S. Horn , D Reago, *Proceedings SPIE* 4130, 226 (2000).

[3.7] M. Z. Tidrow, W. A. Beck, W. W. Clark, H. K. Pollehn, J. W. Little, N. K. Dhar, P. R. Leavitt, S. W. Kennedy, D. W Beekman, A. C. Goldberg, W. R. Dyer, *Opto-Electronics Review* **7**, 283 (1999).

[3.8] M. N. Abedin, T. F. Refaat, I. Bhat, Y. Xiao, S. Bandara, S. D. Gunapala, *Proceedings SPIE* 5543, 239 (2004).

[3.9] P. McCarley, *Proceedings SPIE* 4288, 1 (2001).

[3.10] J. T. Caulfield, *Proceedings of the 32nd Applied Imagery Pattern Recognition Workshop*, IEEE, New York, 2003.

[3.11] F. Capasso, C. Gmachl, R. Paiella, A. Tredicucci, A. L. Huntchinson, D. L. Sivco, J. N. Baillaargeon, A. Y. Cho, H. C. Liu, *IEEE Journal of Selected Topics in Quantum Electronics* **6**, 931-947 (2000).

[3.12] V. W. S. Chan, Optical space communication, IEEE J. Select. Topics Quantum Electronics 959 - 975 (2000).

[3.13] H. Lim., W. Zhan, S. Tsao, T. Sills, J. Szafraniec, K. Mi, B. Movaghar, M. Razeghi, *Physical review B* **72**, 085332 (2005).

[3.14] D. Long, *Infrared Physics* **7**, 169-170 (1967)

[3.15] R. C Jones, *Proceedings IRIS* **2**, 9-12 (1957).

[3.16] R. C. Jones, *Journal of the Optical Society of America* **50**, 1058 (1960).

[3.17] P. Martyniuk, A Rogalski, *Progress in quantum Electronics*, **32**, 89 (2008).

[3.18] M. Aria, M. Zandin, J. G. Pasko, J. Bajaj, L. J. KozlowskI, W. E. Tennant E R. E. De Wames, Proc. SPIE **2274**, 2-16 (1994).

[3.19] G. Destefanis, P. Audebert, E. Mottin E P.Rambaud, Proc. SPIE **3061**, 111-116 (1997).

[3.20] P. Tribolet, J. P. Chatard, P.Costa e A. Manissadjian, *J. Crystal Growth* **184**, 1262-1271 (1998).

[3.21] B.F. Levine, *J. Appl. Phys*. **74**, R1-R81 (1993).

[3.22] M. Razeghi, M. Erdtmann, C. Jelen, F. Guastavino, G. J. Brown, Y. S. Park, , Infr. Phys. and Technol. **42**, 135-148 (2001).

[3.23] E. Towe e D. Pan, IEEE J. Selec Top. Quantum Electr. **6**, 408-421 (2000).

[3.24] V.Ryzhii, , Semiconductor Science and Technol. **11**, 759 (1996).

[3.25]J. Phillips, K. Kamath, and P. Bhattacharya, *Appl. Phys. Lett*. **72**, 2020 (1998)

[3.26] R. Ferreira, G. Bastard, Appl. Phys. Lett. **74**, 2818 (1999).

[3.27] V. Ryzhii, V. Pipa, I. Khmyrova, V. Mitin, M. Willander, Jpn. J. Appl. Phys. **39**, 12B L1283 (2000).

[3.28] H. Lim, S. Tsao, W. Zhang, M. Razeghi, Applied Physics Letters **90**, 131112 (2007).

[3.29] J. Phillips, P. Bhattacharya, S. W. Kennerly, D. W. Beekman e M. Dutra, IEEE J. Quantum Electron. **35**, 936 (1999).

[3.30] M. R. Matthews, R. J. Steed, M. D. Frogley, C. C. Phillips, R. S. Attaluri, S. Krishna, Appl. Phys. Lett. **90**, 103519 (2007).

[3.31] V. M. Apalkov, Physical Review B **75**, 035339 (2007).

[3.32] R. J. Warburton, Comtemporary Physics **43**, 351 (2002).

[3.33] G. Ariyawansa, A.G.U.Perera, X.H.Su, S. Chakrabarti, P. Bhattacharya, Infrared Physics and technology **50**, 156 (2007).

[3.34] Q. Han, X. H. Yang et al., “1.55 μm GaInNAs resonant-cavity-enhanced photodetector grown on GaAs”, Applied Physics Letters **87**, 111105 (2005); para um artigo de revisão anterior veja M. S. Unlu, S. Strite, *Resonant cavity enhanced photonic devices*, Journal of Applied Physics **78**, 607 (1995).

[3.35] M. Gong, K. Duan, C. Li, R. Magri, G. A. Narvaez, L. He, *Physical Review B* **77**,045326 (2008)

4. THEORETICAL MODELING

4.1 Introduction

Theoretical calculations of the energy levels and the oscillator strengths of the several possible transitions are essential for the full understanding of the physics behind the devices based on semiconductor quantum dots. If we want to calculate the electronic band structure to describe a semiconductor, all we have to do is to solve Schrödinger's equation for the system.

To calculate the energy levels in three-dimensional quantum confinement structures, José Maria Villas Bôas, during his short post-doctoral work at *Universidade Federal de Minas Gerais* – UFMG, and Carlos A. Parra Murillo, during his master studies at UFMG, developed a computer code based on the method proposed by Gangopadhyay and Nag [4.1]. In this chapter I briefly explain the method. More details are available in Carlos A. Parra Murillo's master thesis [4.2] and in the original paper.

4.2 Description of the Method

To calculate the energies values and eigenfunctions of the quantum dot photodetector structures, we must solve the Schrödinger's equation in the effective mass approximation for the system:

$$\hat{H}|\,\psi\rangle = E|\,\psi\rangle \tag{4.1}$$

where $\hat{H}$ is the Hamiltonian operator of the complete system.

We consider the single-particle Hamiltonian H, which can be written as:

$$-\left(\nabla \frac{m_e}{m^*(\vec{r})} \cdot \nabla\right) \psi(\vec{r}) + V(\vec{r})\psi(\vec{r}) = E\psi(\vec{r}) \tag{4.2}$$

where m_e is the free-electron mass, $m^*(\vec{r})$ is the effective electron mass for the structure , and V is the potential.

We can write $\psi(\vec{r})$ in a convenient basis of functions:

$$\psi(\vec{r}) = \sum_i a_i g_i(\vec{r}) \tag{4.3}$$

The basis functions are the solutions $(\hat{H}_0| g_i\rangle = E_i| g_i\rangle)$ of the problem consisting of one particle with effective mass m_e confined in a large cylinder of radius R and height L and a potential V = 0, if r < R, and infinity otherwise (Figure 4.1). For this problem we find that:

$$E_{lmn} = \frac{\hbar^2}{2m_e}\left(\frac{n^2\pi^2}{L^2} + \frac{k_{lm}^2}{R^2}\right) \tag{4.4}$$

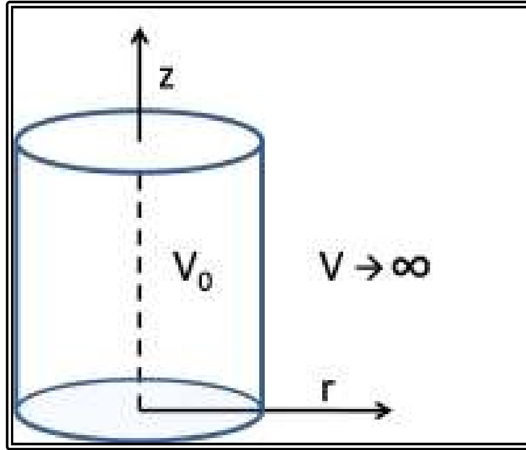

Figure 4.1: Schematic representation of H_0 used to construct the basis for H.

The second step consists of studying a quantum dot structure placed inside a cylinder like the one in Figure 4.1. For this we solve the eigenvalue equation 4.5, where H contains all the information about the quantum dots and barriers.

$$\hat{H}| \psi\rangle = E| \psi\rangle \tag{4.5}$$

For this purpose we implemented the method introduced by Gangopadhyay and Nag [2]. If we substitute equation 4.3 in equation 4.2 and multiply the result by $g^*_{l'm'n}$ and integrate in all the space we obtain a characteristic equation:

$$\sum(A_{l'm'n',lmn} - E\delta_{l'l}\delta_{m'm}\delta_{n'n})\, a_{l'm'n'} = 0 \tag{4.6}$$

The matrix elements are given by:

$$A_{l'm'n',lmn} = -\iiint_{space} dV \left(g^*_{l'm'n} \cdot \frac{m_e}{m^*}\nabla^2 g_{lmn} - g^*_{l'm'n} V g_{lmn} \right) \tag{4.7}$$

It is possible to reduce the expression of the matrix elements integrating by parts the left term in the parenthesis, so we obtain:

$$A_{l'm'n',lmn} = -\iiint_{space} dV \left(\frac{m_e}{m^*}\nabla g^*_{l'm'n} \cdot \nabla g_{lmn} - g^*_{l'm'n} V g_{lmn} \right) \tag{4.8}$$

To solve the equation above it is important to note that:

1) the effective mass is a function of r and z,
2) the structures studied here have discontinuous effective mass, and,
3) the structures studied here have discontinuous potential functions at the interfaces between two different materials.

To solve equation 4.8 we consider the following:

i) We integrate with $m^*(r, z) = m_b$ and $V(r, z) = V_b$ over the external cylinder because ψ is null outside the cylinder. This gives us:

$$\left[A^{Cyl}_{l'm'n'lmn}\right]_{m_b,V_b} = \left(\frac{m_e}{m_b}\left(\frac{k^2_{lm}}{R^2} + \frac{n^2\pi^2}{L^2}\right) + V_b\right)\delta_{l'l}\delta_{m'm}\delta_{n'n} \tag{4.9}$$

ii) Then, in the last term, we subtract the integral over the region where the quantum dot is located and we add the same integral but with the

quantum dot parameters, i.e, m*(r, z) = m_{QD} e V (r, z) = V_{QD} (see Fig. 4.2), this gives:

$$[A^{QD}_{l'm'n'lmn}]_{m_b,V_b} - [A^{QD}_{l'm'n'lmn}]_{m_{QD},V_{QD}} = \iiint_{QD} dV \left(\frac{m_e}{m_{QD}} - \frac{m_e}{m_b}\right) \nabla g^*_{l'm'n} \cdot \nabla g_{lmn} + \iiint_{QD} dV \left(V_{QD} - V_b\right) g^*_{l'm'n} g_{lmn} \quad (4.10)$$

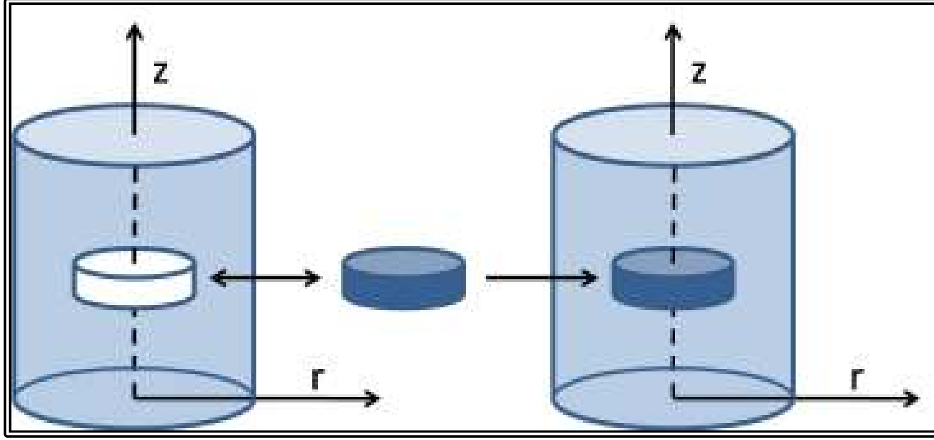

Figure 4.2: Schematic representation.

iii) so, the matrix element A can be written as:

$$A^{Total}_{l'm'n'lmn} = [A^{cyl}_{l'm'n'lmn}]_{m_b,V_b} + [A^{QD}_{l'm'n'lmn}]_{m_b,V_b} - [A^{QD}_{l'm'n'lmn}]_{m_{QD},V_{QD}} \quad (4.11)$$

In our project, we studied several complex structures with quantum wells, barriers and quantum dots inserted in the structure. To compute real structures we generalize this process. So, if the structure consists of N dots and M wells, the matrix element is given by (see Figure 4.3):

$$A^{Total}_{l'm'n'lmn} = [A^{cyl}_{l'm'n'lmn}]_{m_b,V_b} + \sum_{i=0}^{N}\left([A^{QD_i}_{l'm'n'lmn}]_{m_b,V_b} - [A^{QD_i}_{l'm'n'lmn}]_{m_{QD_i},V_{QD_i}}\right) + \sum_{i=0}^{M}\left([A^{well_i}_{l'm'n'lmn}]_{m_b,V_b} - [A^{well_i}_{l'm'n'lmn}]_{m_{well_i},V_{well_i}}\right) \quad (4.12)$$

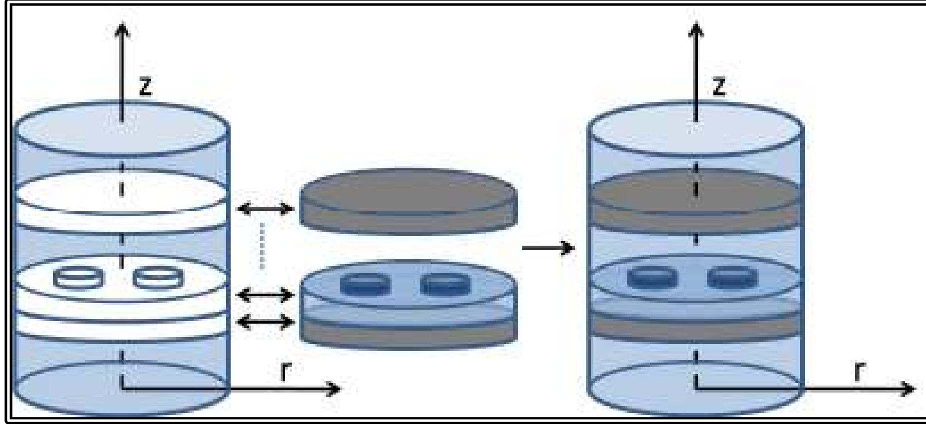

Figure 4.3: Schematic representation of H_0 used to construct the basis for H in the case of several dots and wells in the structure.

iv) Up to now I show how to solve the matrix elements for an arbitrary quantum dot shape. Here we show how to include the quantum dot shape in the equation. For this, we go back to equation 4.12 and modify the integral limits and in this way it is possible to change the dot shape. The most common shapes are shown is Figure 4.4. In this picture we show the curve that generates the quantum dot by the rotation of this plane along the z-axis. This defines the upper limit of the integral.

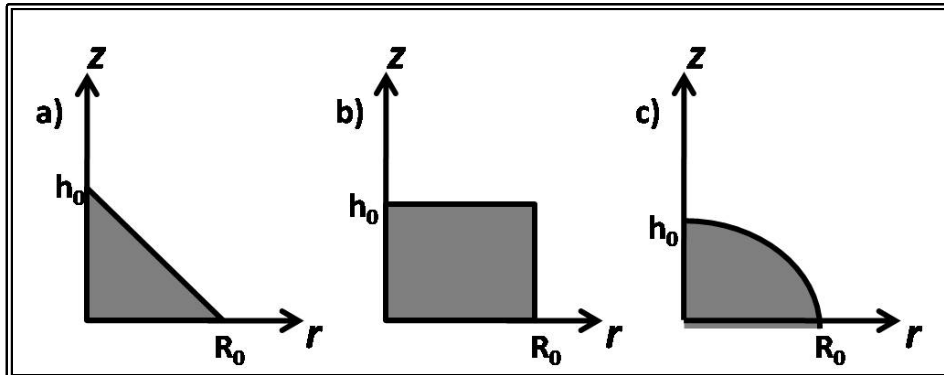

Figure 4.4: Different quantum dot (QD) shapes. In (a) cone shaped QD, in (b) cylinder shaped QD and in (c) lens shaped QD.

For the QD shapes shown in Figure 4.4 the upper limit of the integral is wrriten as:

1) Cone shaped QD:

$$z(r) = h_0\left(1-\frac{r}{R_0}\right) \tag{4.13}$$

2) Cylinder shaped QD:

$$z(r) = \begin{cases} h_0, & 0 \le r \le R_0 \\ 0, & otherwise \end{cases} \tag{4.14}$$

3) Lens shaped QD:

$$z\,(r) = h_0\sqrt{1-\frac{r^2}{R_0^2}} \tag{4.15}$$

v) The next important parameter to compute is the oscillator strength for each pair of levels, which allows us to find the most probable intraband transitions in the system, due to absorption of incident radiation. To compute this parameter the most frequently used formula is:

$$f(l',k';l,k) = \frac{2m^*}{\hbar^2}\,(E_{l',k'} - E_{l,k})\,|\,\langle l',k'|\vec{r}|l,k\rangle\,|^2 \tag{4.16}$$

Its use depends on the system of units used, but what are really important are the relative values between the transitions. The difficulty in this point is to calculate the matrix element of the position vector $\vec{r}$. In our case we have that:

$$\begin{aligned}\langle l',k'|\vec{r}|l,k\rangle &= \int_V d\vec{r}\ \langle l',k'|\vec{r}|\vec{r}\rangle\,\langle\vec{r}|l,k\rangle \\ &= \int_V d\vec{r}\ \left(x\hat{\imath}+y\hat{\jmath}+z\hat{k}\right)\langle l',k'|\vec{r}\rangle\langle\vec{r}|l,k\rangle \\ &= \int_V d\vec{r}\ \left(x\hat{\imath}+y\hat{\jmath}+z\hat{k}\right)\psi^*_{l',k'}\ (r,\varphi,z)\,\psi_{l,k}\ (r,\varphi,z)\end{aligned} \tag{4.17}$$

where $\langle\vec{r}|l,k\rangle = \psi_{l,k}\ (r,\varphi,z)$ are the eigenfunctions of our problem.

In Chapter 6 I present the calculated energy levels and oscillators strength for the structures studied in this thesis.

References

[4.1] S. Gangopadhyay, B. R. Nag, Nanotechnology **8**, 14 (1997).

[4.2] Parra Murillo, Carlos. **Study of semiconductor heterostructures with embeded quantum dots: micropillares and photodetectors**. Universidade Federal de Minas Gerais, 16 de julho de 2009**.** Available at http://www13.fisica.ufmg.br/~posgrad/ at Trabalhos finais: Dissertações/2000/Carlos-Parra.

5. EXPERIMENTAL TECHINIQUES

5.1 Fourier Transform Infrared Spectroscopy

The device characterization is based on photocurrent and absorption measurements done with a Fourier Transform Infrared (FTIR) spectrometer [1]. The FTIR spectrometer is based on a Michelson interferometer and consists of a fixed mirror, a moving mirror and a beamsplitter (Figure 4.1). In a continuous-scan mode, the moving mirror moves at a constant velocity, and an optical path difference is generated in time. This optical path difference is called retardation, δ (usually given in cm). The infrared (IR) light (polychromatic source) passes through this interferometer, and generates an interferogram. The interferogram is a superposition of sinusoidal waves at all IR wavenumbers, in units of cm^{-1}. The sample is illuminated with the interferogram and the signal that results (see paragraph below) is then collected by a detector and analyzed by a specific software (OMNIC, from ThermoNicolet), which gives the interferogram I (δ). The signal is Fourier transformed and generates a spectrum as a function of frequency.

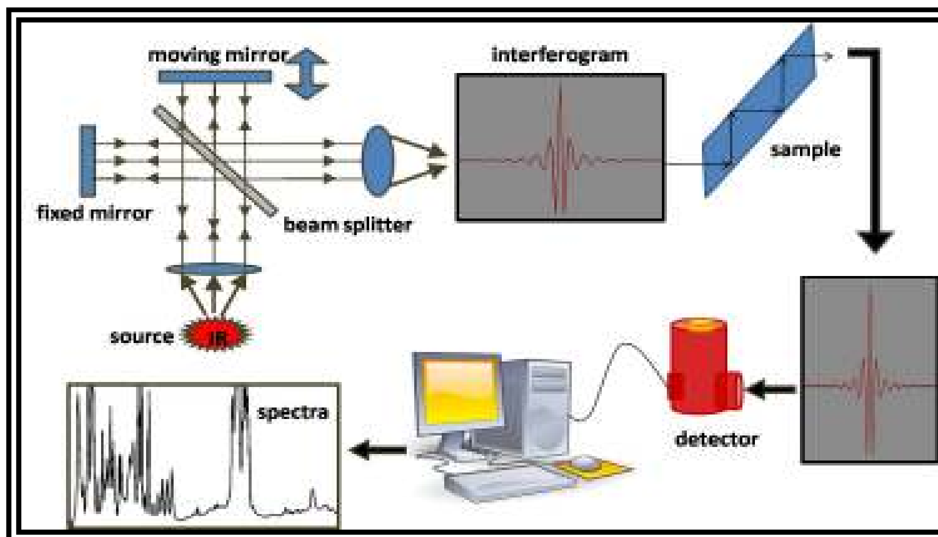

Figure 5.1: Schematic picture of the FTIR setup for absorption measurements.

For absorption measurements the interferogram generated by the interferometer passes through the sample (Figure 5.1) and it is collected by a mercury cadmium telluride (MCT) detector, which supplies a signal proportional to the intensity of the transmitted light which is going to be Fourier transformed. For the photocurrent measurements the detector is the device under study itself. In this case, the signal which will be Fourier transformed is the photocurrent generated by the incident light (interferogram). We use an external setup with mirrors and lenses to focus the radiation in the device, which is placed inside a cryostat to control the temperature. The setup for photocurrent measurements is schematically shown in Figure 5.2. The measurements were done as function of bias, temperature, filters (to block interband excitation) and polarization. The important results are presented in the last chapter of this thesis.

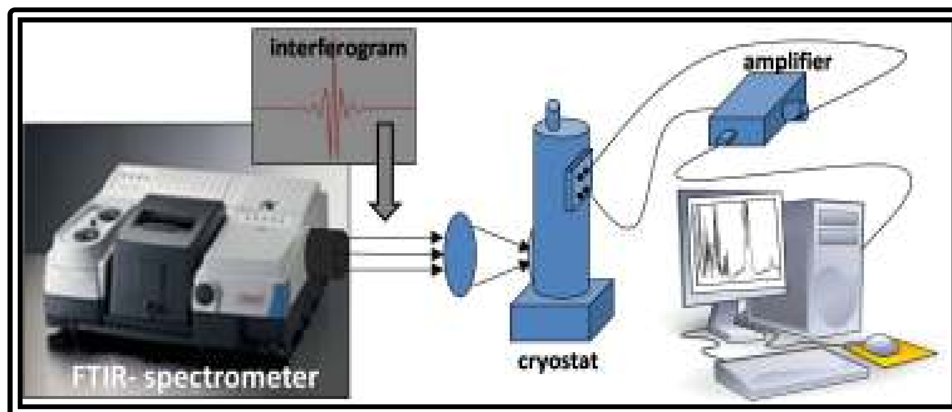

Figure 5.2: Setup for photocurrent measurements

5.1.1 Sample Processing for Photocurrent Measurements

All the samples were processed at the Technical University of Vienna (TU-Wien) during a one year stay (Sandwich PhD scholarship – SWE) in 2008.

The processing of the samples for photocurrent measurements consists on the device fabrication. It is, basically, a sequence of steps to build up the *mesas* with an optical window and also to fabricate the electrical contacts (Figure 3.5). This last step includes the deposition of metal layers to contact the wires. The area of our devices is around 9×10^4 µm², therefore the fabrication procedure is very delicate.

There exist different methods and recipes for processing the devices, which depend on the device size, thickness and material, and also on the clean room equipment facilities. The processing of the samples studied here was done by conventional photolithography and dry etching. The sequence of steps and parameters are described in this section.

The etch of the InP was done at a temperature of 250 ^{0}C. Therefore, we cannot use conventional polymer resists as protection for the etch. Instead, we use SiN. So, the first step of the processing consists on depositing a SiN layer on the sample. The deposition was done in a Plasma Enhanced Chemical Vapor Deposition (PECVD) chamber. This process allows the deposition of thin films from a gas phase on a substrate. The deposited thickness was 600 nm, and it was controlled by the gas flux, power and deposition time.

The second step is the transfer of the pattern of the mask to the SiN. For that we use conventional photolithography with the 5214 Photo-resist. We deposit the resist on the sample located in a spinner, rotating at 10 thousand rotations per minute during 35 seconds, to achieve a 1.1 µm thickness. Then we bake the resist for 1 minute at 120°C. In the mask aligner, we illuminate the sample during 4.5 seconds, and in the sequence we develop for 30 seconds in AZ 351 solution. A schematic picture of the sample at this point of the processing is shown in Figure 5.3 b).

The following step is the etching of the SiN, to transfer the pattern of the resist layer to the SiN. The etching was done with a Reactive Ion Etching (RIE) system with a step and strike pressure of 15 and 40 mtorr, respectively and power of 60 W at 25 ^{o}C. The gas used was SF_6 at a flux of 40 sccm. After this step, the sample looks like shown schematically in Fig. 5.3 c).

To start etching the sample, to build up the mesas, it is necessary first to remove the resist layer. This procedure was done in a *Tepla* plasma oxidation machine, which removes only organic materials. See Fig. 5.3 d)

The sample etching was done at 250 ^{0}C in a Reactive Ion Etching (RIE) setup,with SiCl4 and Ar with a flux of 5 and 40 sccm. The step and strike pressures were 2 and 40 mtorr respectively and the power was 200 W (Fig. 5.3 e).

The next procedure is to remove the SiN and prepare the sample for metallization. The SiN was removed in the same way it was etched (Fig. 5.3 f).

The following photolithography, to select the metallization area, was done with a negative resist, MAN 440, spinning the resist at 6000 rotations per minute during 30 seconds. The sample was warmed for 5 minutes at 95°C before being taken to the mask aligner. The exposure time in the mask aligner was 60 seconds. The developer used was MAD 333 for 70 seconds.

The sequence of metals used for the fabrication of the ohmic contacts was Ti (100Å), Au (50Å), Ge (30Å), Ni (100Å) and Au (2000Å).

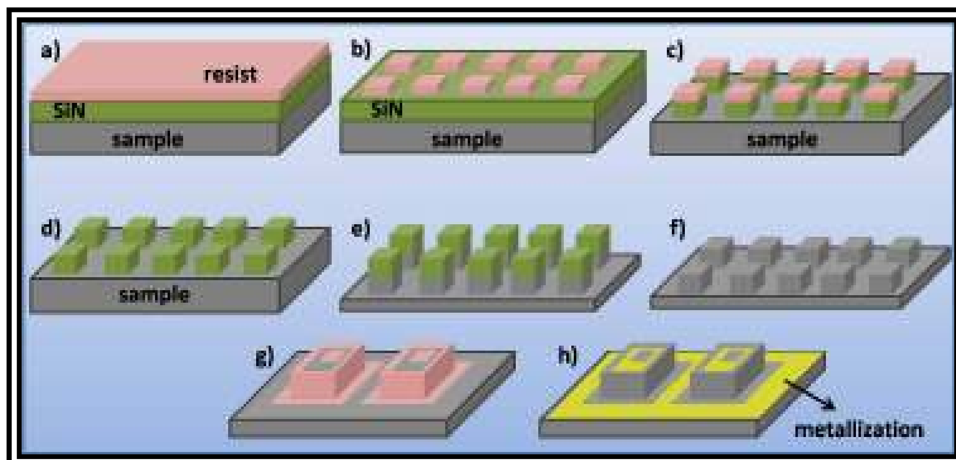

Figure 5.3: Illustrative picture of the sample for all the process steps.

5.1.2 Sample Processing for Absorption Measurements

For absorption measurements the samples were processed in a waveguide geometry to increase de optical pass inside the sample and consequently to achieve a better signal to noise ratio. Still aiming a better signal, we used samples with 20 periods in the active region (for photocurrent measurements the samples had only 10 periods).

The waveguide geometry consists on polishing the facets of the samples in 45º and focus the light on this facet. Thus the incident radiation suffers multiple internal reflections (Figure 5.4), increasing the optical path inside the material.

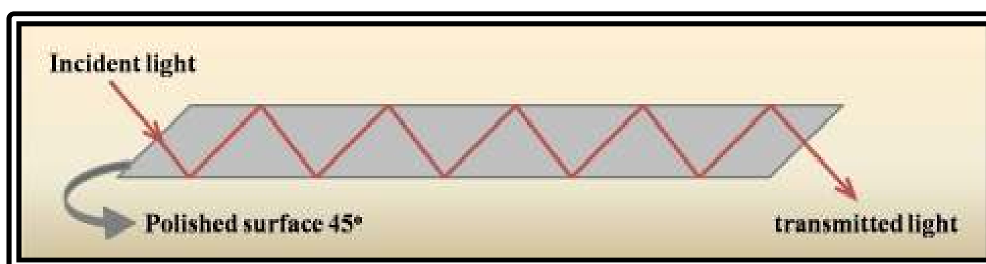

Figure 5.4: waveguide geometry.

To achieve a good facet quality the polishing was initiated with P1200 paper and finished with diamond paste of 1μ m. In this way we ensure that the incident radiation is not significantly scattered by the surface. To measure the absorption of the samples in the mid-infrared we use the setup schematically show in Figure 5.1.

In order to polish a waveguide the samples were fixed on a well designed metallic sample holder.

5.2 Current-Voltage Measurements

The current-voltage (IV) measurements were done with a HP4155B parameter analyzer. The samples were mounted inside an optical cryostat to perform temperature dependent measurements. The measurements were performed under dark condition, from V = -5 V to V= +5 V in steps of 10 mV and the maximum current (compliance) was 100 mA.

Figure 5.5 shows the IV curves for the QD-undoped sample described in section 6.2 and in Figure 5.6 the IV curves for the sample 6.3.

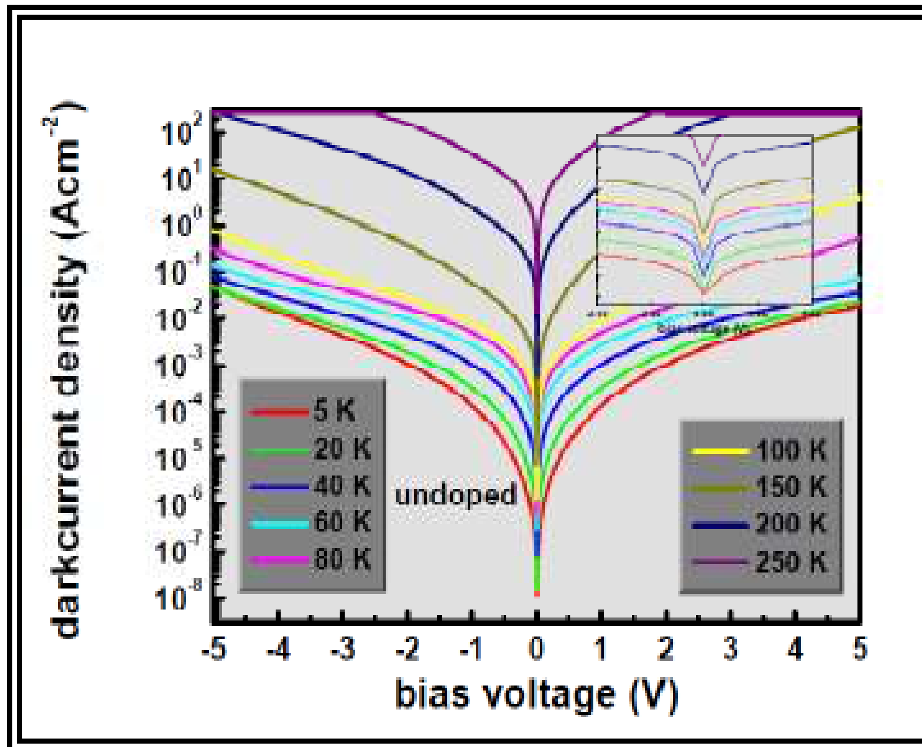

Figure 5.5: IV curves of the InAs/InP undoped QD sample as function of temperature. The inset is a zoom close to zero bias.

The IV curves are symmetric for positive and negative bias voltage up to 60 K, where the current starts to become larger for positive bias. No built-in field can be observed for small bias voltages as can be seen in the inset of the IV-graph.

References:

[5.1] Advanced FT-IR spectroscopy, Eric Y. Jiang, Thermo Electron Corporation.

6. RESULTS

6.1 Introduction

In this Chapter the most important results obtained during this PhD are shown. I studied around 20 quantum dot samples for infrared photodetection, all of them based on InAs quantum dots (QDs) grown on InGaAlAs material lattice matched to InP and covered with InP. We begin the studies with simpler samples, only the InAs QDs and the InP barrier. In this first set of samples we vary the quantum dot doping to achieve the best signal to noise ratio. In the second set of samples we investigate an alternative structure where a InGaAs quantum well (QW) is included. It is difficult to reproduce exactly the shape and size of self-organized QDs and it is not trivial to determine how the QD morphology affects the spacing between energy levels. Small variations in the structure cause changes in the range of detection of the photodetector [6.1]. In an attempt to minimize these difficulties, these alternative structures where self-organized quantum dots are embedded in quantum wells were suggested [6.2]. These structures, usually called dots in a well (D-WELL) provide a degree of control over the final energy state of the transition. In this way one can control the wavelength of detection mainly by controlling the spacing between energy levels by varying the composition and / or the thickness of the potential well. After that, we checked how the InP barrier influences the photoresponse. For that we grew samples with three different thickness of the barrier. This work is detailed in section 6.3. Later on we tried the, namely, T-QDIPs (tunneling QDIPs) structures. For this study we include double InAlAs barriers (Figure 6.12) in the structure. Ariyawansa *et al.* [6.3] was the first one to study this kind of QDIPs, but in their case the structure was lattice matched to GaAs. As I said in the Introduction of this thesis, the lattice mismatch of the InAs/InP system is smaller when compared to the InAs/GaAs system. The double barriers in the T-QDIPs are supposed to block the dark current and the transport of carriers is done by tunneling, improving the efficiency of the device.

In the sections below I present some physical processes involved in the structures developed for this thesis.

6.2 Evidences of Intraband Auger Process in Quantum Dot Infrared Photodetectors

For most of the QD structures used for infrared photodetection, the optical transitions are intraband and occur between two bound states or a bound and a quasibound state. The physical process behind the carrier extraction from the excited states to generate the observed photocurrent (PC) is often attributed to thermal excitations, even for deep final bound states [6.4-6.7]. Another mechanism to extract the carriers to the continuum, where they can contribute to the PC, is via an Auger process. This physical phenomenon is based on energy exchange between electrons. When an electron in a high energy level falls to a lower energy level, the excess energy can be transferred to a second electron. If this energy is enough to promote it to the continuum, this second electron, the Auger electron, might be collected contributing to the PC.

The importance of Auger processes in semiconductor quantum dot structures has already been claimed in the 90's in a detailed theoretical study [6.8]. More recently, the interband PC spectra of InAs quantum dots embedded in an InP matrix were explained by the involvement of Auger processes [6.9] in undoped layers and n- and p-type doped InGaAs quantum dots were theoretically investigated [6.10]. However, the first experimental evidence of the Auger effect on intraband transitions in QDIPs was investigated by our group [6.11]. In this section I present our results that demonstrate that Auger processes seem to play a fundamental role in generating an intraband PC.

In order to observe the Auger effect in intraband transitions in QDs, samples were designed in such a way that there awere several bound states available inside the dot. This can be achieved by growing relatively large dots.

The samples prepared for this study were grown by MOVPE (see Chapter 2) on a 150 nm thick InP buffer layer deposited at 630°C on a semi-insulating InP substrate followed by a 500 nm thick n-doped lattice matched InGaAs layer acting as the bottom contact. Then a 109 nm thick lattice matched layer of InGaAlAs is grown with 16% Al

content. The InAs QDs are then deposited for 5.5 s at 520°C and annealed in an arsine atmosphere for 12 s. They are covered by a 13 nm thick InP layer while the temperature is ramped up to 600°C. This sequence is repeated 10 times. A last 109 nm thick layer of the quaternary material is then grown and finally a 250 nm *n*-doped InGaAs contact layer is deposited. The doping level at the contact layers is 1.0 x 10^{18} cm^{-3}. All ternary and quaternary layers are grown at 600°C. The QD samples were grown with three different doping levels: one nominally undoped sample and 2 samples with a doping which corresponds to approximately 2 and 4 electrons per dot, respectively. The schematic conduction band potential profile and scheme of the samples are presented on Figure 6.1.

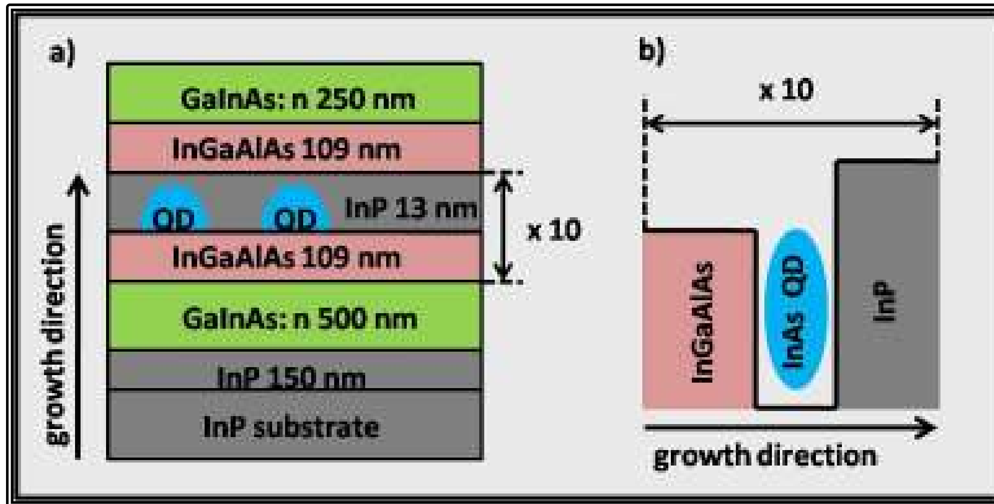

Figure 6.1: a) shows schematically the layers material and thickness along the growth direction and in b) the conduction band profile of one period of the active region.

Atomic force microscopy (AFM) was performed and an average dot height and density of 9 nm and 1.5 x 10^{10} cm^{-2}, respectively were measured on uncapped QD control samples [6.12]. Transmission electron microscopy (TEM) images showed lens shaped QDs with a base diameter of approximately 60 nm and confirmed the QD height average of 9 nm. The images are shown in Figure 6.2.

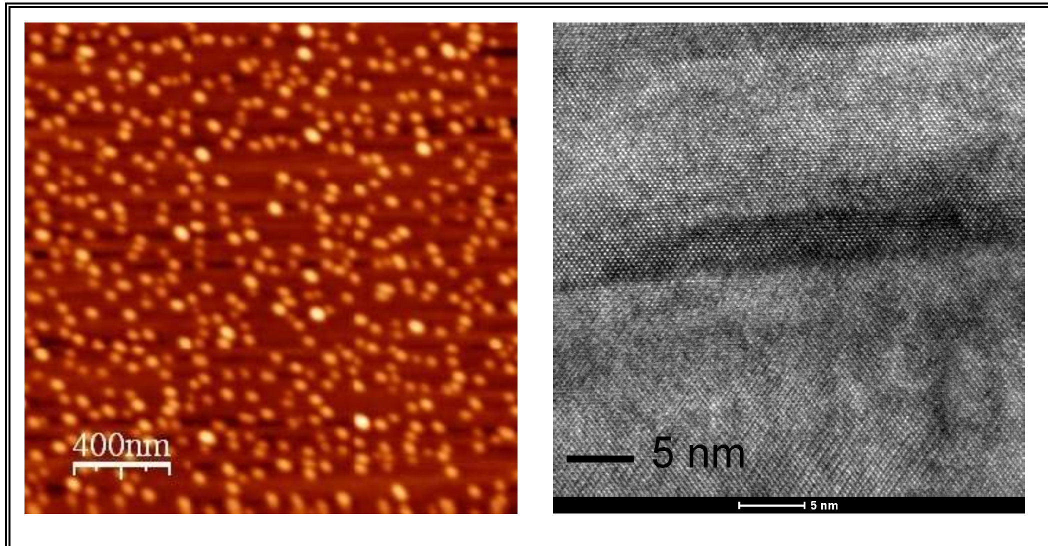

Figure 6.2: AFM (left side) and TEM (right side) images of the quantum dot structures.

To characterize the devices, photocurrent measurements were performed using Fourier Transform Infrared Spectroscopy (FTIR) (see chapter 5). Figure 6.3 shows the photocurrent spectra at 5 K for the investigated samples measured with normal incident light and no external bias. A narrow PC peak is observed around 190 meV for the undoped sample. The sample is nominally undoped, but the presence of residual doping and carrier diffusion from the contacts lead to a population inside the QD so that intraband transitions can occur. A stronger and broader signal was observed for the doped samples. The broadening of the PC peak with the doping is due to the inhomogeneous size of the quantum dots all over the structure. For larger QDs, the ground state lies deeper in energy, so for the undoped sample, only part of these dots is populated, originating a narrow PC peak. For the doped ones, also the smaller dots have electrons inside and this small difference in energy is responsible for the broadening of the PC peak.

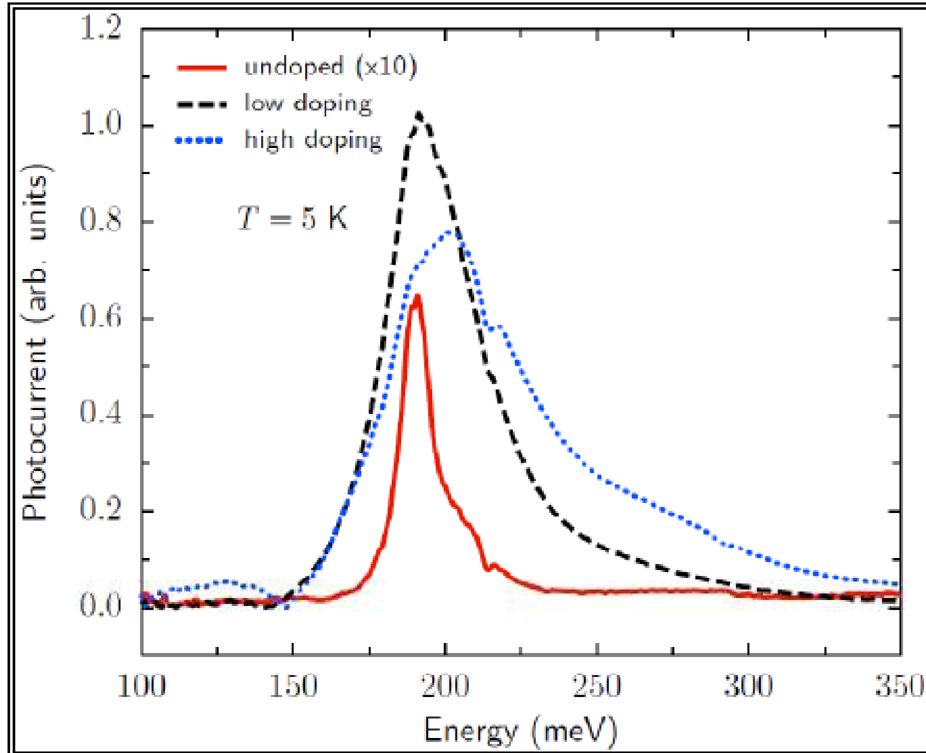

Figure 6.3: Photocurrent spectra for all three samples. The inset shows the absorption spectra around 200 meV for the undoped and high doping samples.

Absorption measurements were performed as a complementary characterization technique to confirm the observed transition (Figure 6.4). The experiment was performed in the waveguide geometry (section 5.1.2) using the same type of structures as for the PC measurements but with 20 periods in the active region instead of 10 periods and without the InGaAs contact layers. A peak centered around 190 meV is observed in agreement with the PC spectra. This technique was essential to confirm the involved transition observed in the PC measurements as it is a direct measurement of the electronic transition. In the case of PC, the carrier extraction is also involved. A schematic picture of the FTIR setup for absorption measurements is presented in Figure 5.1.

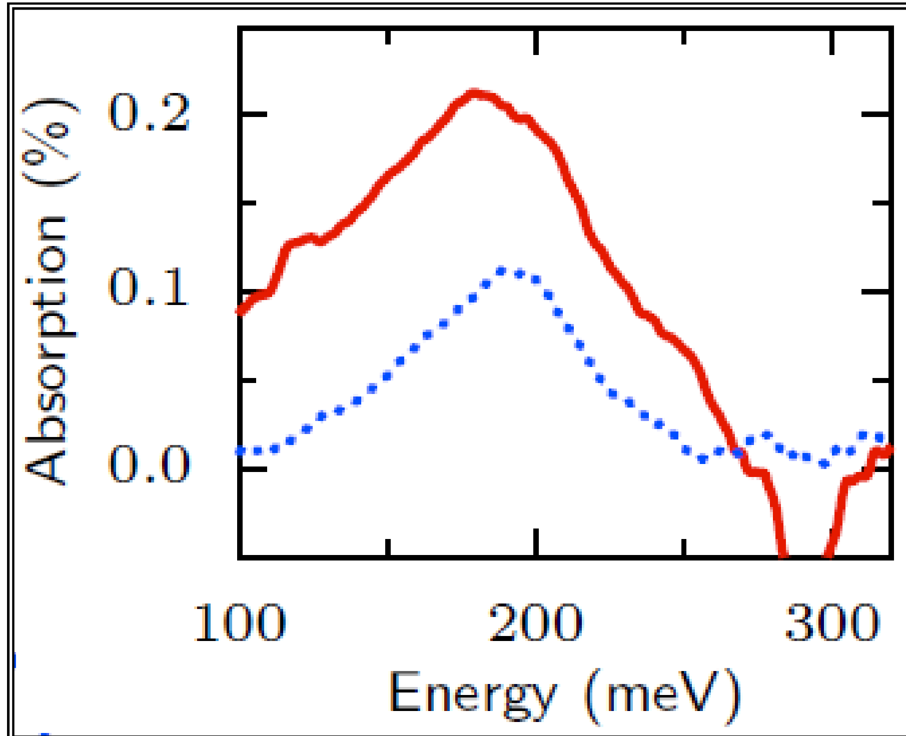

Figure 6.4: Absorption measurements for the undoped sample (red spectra) and the high doped sample (blue spectra).

To calculate the energy levels of the structure and identify the transitions responsible for the PC, a 3D effective mass model, described in Chapter 4, was used [6.13]. The results of the calculations can be seen in Figure 6.5 where the solutions for the azimuthal quantum numbers 0 (solid line) and 1 (dashed line) are superimposed on the QD potential profile. The transitions with the higher oscillator strength are between the ground state and the fourth excited state for m=0 and m=1, corresponding to 187 and 197 meV, respectively. An interesting observation is that the final state of this transition is 200 meV below the continuum of energy levels, and so, these excited electrons could not directly generate the observed PC, measured at a temperature of 5 K.

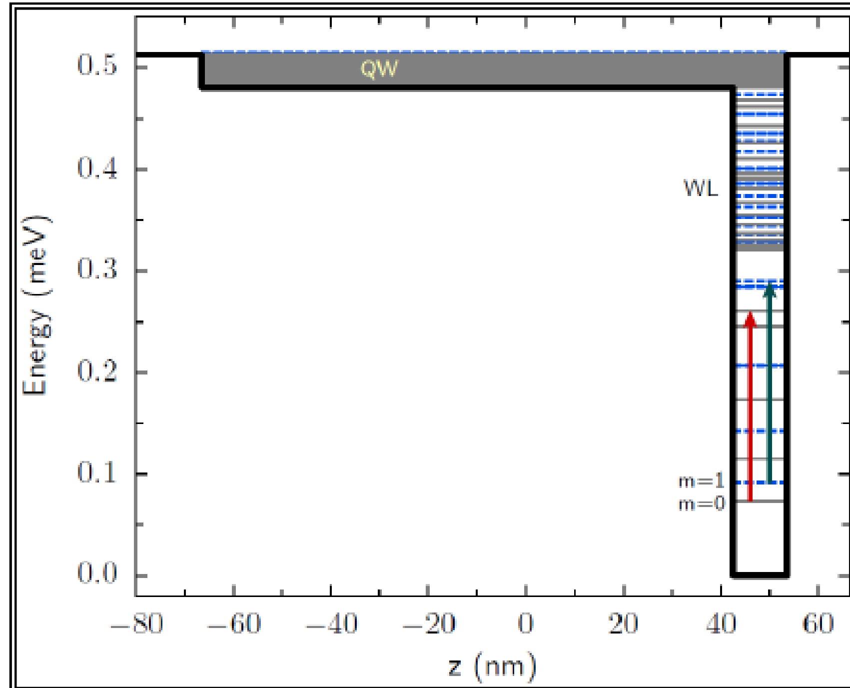

Figure 6.5: Calculated energy levels superimposed on the conduction band profile of one period of the active layer of the samples. The arrows represent the transitions with the highest oscillator strength.

The generation of the PC is attributed to an Auger process where one electron, previously in an excited level, relaxes to the ground state transferring its energy to a second electron, on the final state of the absorption, which can be excited to a higher energy state in the continuum. A scheme of such a mechanism is shown in Figure 6.6.

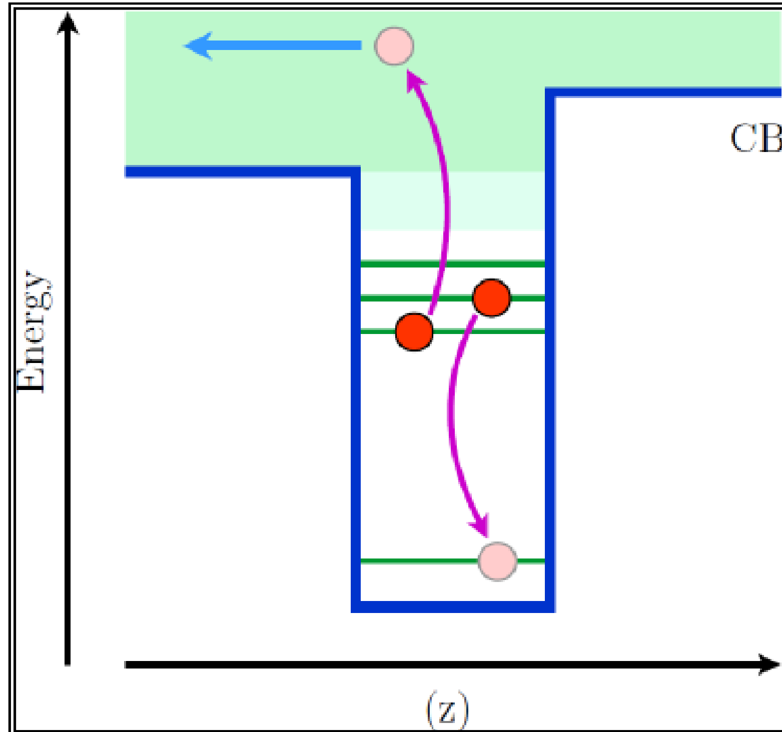

Figure 6.6: Schematic picture of an intraband Auger process.

Some further results support the attribution of an Auger process as the one responsible for the generation of the observed PC. The first one can be seen in Figure 6.7, where the spectra of the PC for temperatures up to 80 K are shown. The intensity of the PC as a function of temperature is nearly the same up to 60 K. This means that the thermal energy is not enough to extract the carriers from the final absorption state within the dot, increasing the PC signal.

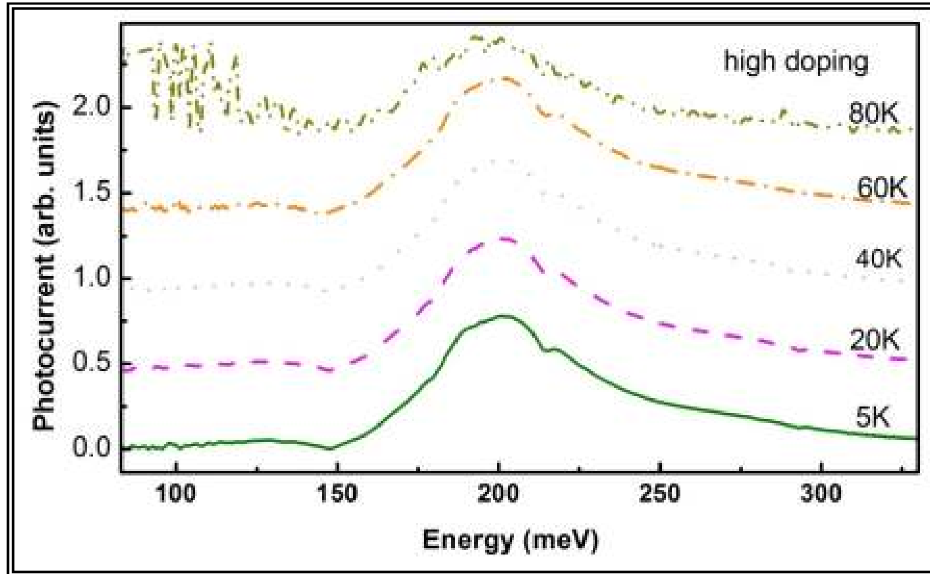

Figure 6.7: Photocurrent measurements at different temperatures. The spectra are shifted vertically for clarity.

Another analysis that supports the fact that the PC is produced even though the final state of the absorption is a deep bound state can be made by comparing the photoluminescence (PL) (Figure 6.8, dashed line) with the interband PC (solid line) at 80 K. The PL shows a peak centered around 700 meV due to recombination of the electron-hole pair in the QD. At the same energy, the interband PC can be seen implying that the electrons excited from the valence band to the lowest electron state produce a current. As has been claimed by Landin et al., in Ref. 6.9, the interband PC from the QDs is produced by an interband Auger effect, where the photo-excited electron receives additional energy from the recombination of another electron with the photo-generated hole. A scheme of such a process is depicted in the inset of Figure 6.8. The strong peak starting around 1 eV in Figure 6.8 is due to the interband PC in the InAlGaAs material.

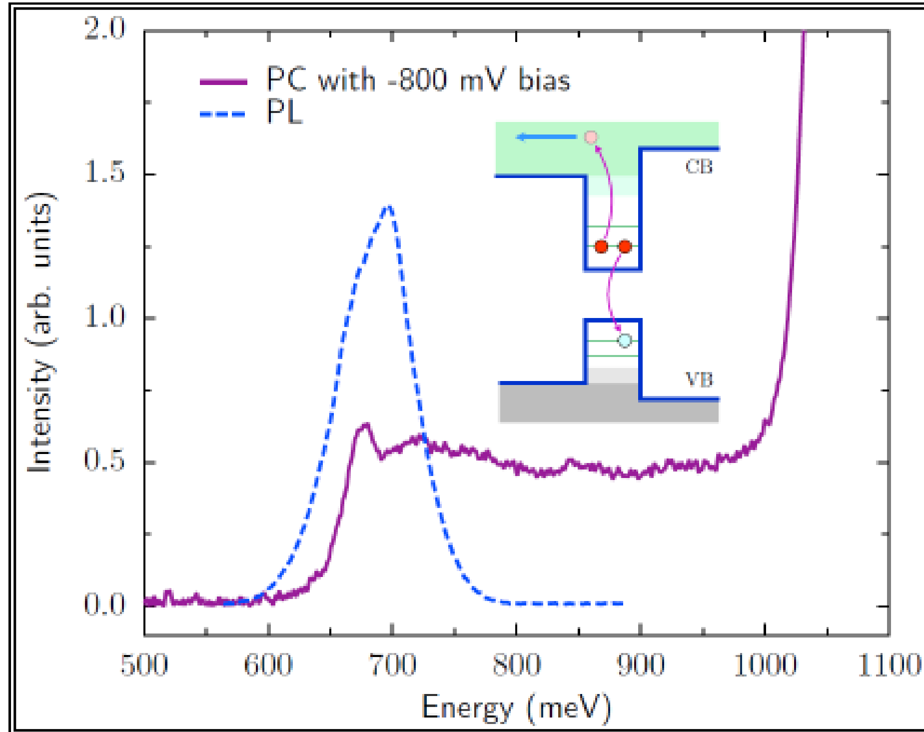

Figure 6.8: Photoluminescence and interband photocurrent measurements and a schematic picture of an interband Auger process.

The difference between the intraband and interband Auger effect is that for the first one it is necessary to have two electrons in the excited states, in the same quantum dot and essentially at the same time. Even though it can appear improbable, it is necessary to remember that the FTIR measurements are performed with a broadband source, implying that several different absorptions can occur simultaneously.

Another explanation for the Auger mediated transfer of the electrons from the upper bound state to the continuum is the presence of dynamical processes in the device which could cause a non-vanishing population of higher states. The dark current in the devices is a result of thermal emission and re-capture of electrons. Time-resolved measurements performed by other members of our group [6.14] demonstrate that electron capture occurs very fast into high lying states and is then slowed down. As a consequence we can expect that higher lying dot states are populated. Thus an excited electron can be promoted to the continuum by an Auger scattering event between a photo-excited electron and a captured electron.

A second configuration for Auger scattering can be found if the effect of the persistent device current is taken into account. As the devices were operated in current-mode, a photocurrent was present even without bias applied due to an intrinsic electric field. When the electrons pass through the QD layers some of them can relax into the dots. If an electron relaxes into a dot with an excited electron inside, this electron can be promoted to the conduction band continuum due to Auger scattering and will contribute to the PC.

The detectivity of these devices was estimated. Figure 6.9 shows the results as function of bias and temperature. One can clearly conclude that the low doping sample shows a better performance, especially at low temperatures and low applied bias voltages. For the responsivity measurements we use an InAs filter to avoid interband population. To calculate the noise we considered the generation-recombination noise I_{GR} which is the dominant noise mechanism in QDIPs and can be estimated by measuring the dark current I_D (see section 3.2.1).

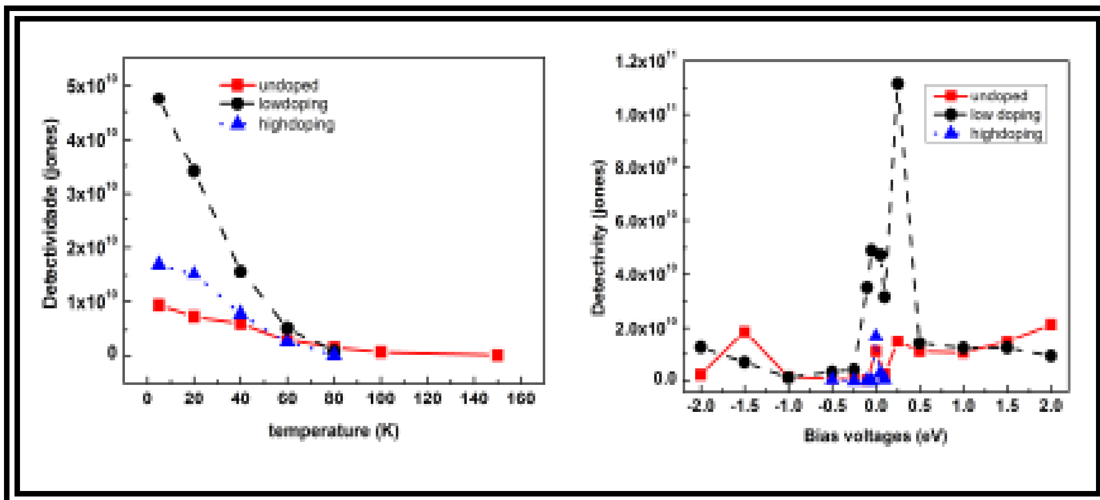

Figure 6.9: Detectivity as function of temperature (left hand side) and bias voltages (right hand side) of all three samples.

In summary, we have presented a detailed study of the intraband optical response in quantum dot structures for mid-infrared photodetection. The obtained photocurrent and absorption results, together with a realistic theoretical calculation,

strongly suggest that an Auger process can produce a significant current. Photoluminescence together with interband photocurrent further supports this attribution. The reported results indicate that quantum dot structures can be designed for the implementation of selective photodetectors based on bound-to-bound transitions, with well defined, sharp, operation energies.

6.3 Very Narrow Band QDIP Operating at 12 μm

Due to discrete energy levels, QDs structures should lead to narrower transitions, desirable for achieving high selective devices. Therefore QDIP structures should be ideal to distinguish two different gases with absorption at wavelengths in the mid infrared which are very close to each other or for sharp temperature discrimination for imaging. For the latter application, devices with operating wavelengths in the 9-12 μm range should be employed since they correspond to maximum of the thermal emission at room temperature and peak widths as narrow as possible are desirable. In this section I present the development of an InGaAlAs/InGaAs/InGaAlAs/InAs/InP QDIP structure where an InGaAs quantum well is coupled to the InAs quantum dots which operates around 12 microns with a photocurrent peak as narrow as 5 meV (5% for $\Delta\lambda/\lambda$). The absorption occurs between deep quantum dot states and the current generation, which is mediated by Auger scattering [6.11], relies on tunneling through an adjacent quantum well.

The investigated QDIP structures were grown by metalorganic vapor phase epitaxy (section 2.3.2). The active region of the device consists of 10 periods of a 99 nm thick InGaAlAs layer with 16% Al content lattice matched to the InP substrate on which a 10 nm $In_{0.53}Ga_{0.47}As$ quantum well is grown followed by a 3 nm quaternary barrier on top of which the InAs quantum dots are nucleated. The dots are finally covered by an InP barrier with three different thicknesses, namely: 10, 13 and 16 nm. Finally, another 99 nm thick quaternary layer is deposited (See picture 6.10). The entire periodic structure is grown between *n*-doped $In_{0.53}Ga_{0.47}As$ contact layers. The quantum dots are *n*-doped with a density of approximately two electrons per dot.

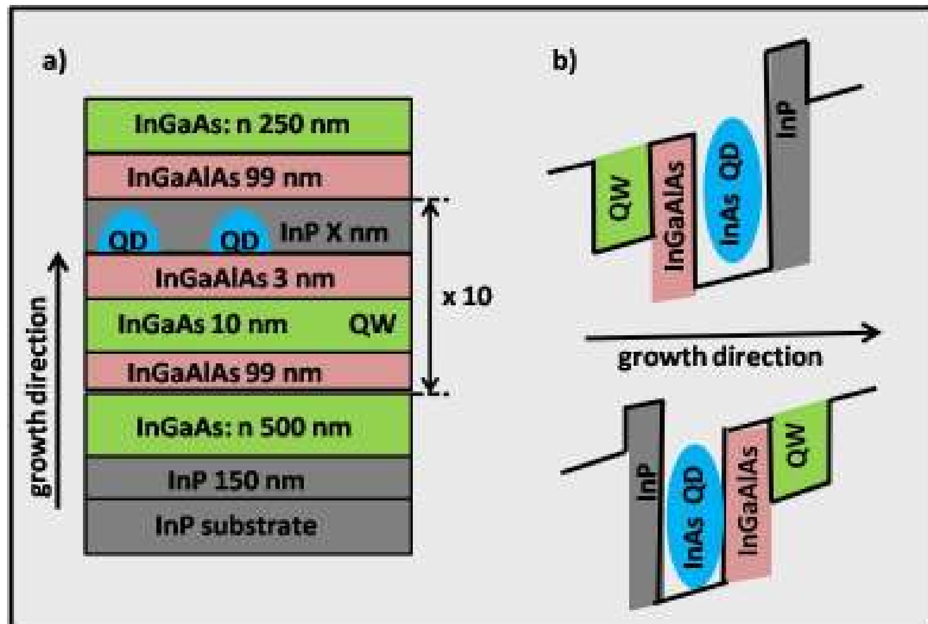

Figure 6.10: a) Sample structure where the thickness of the InP barrier X = 10, 13 and 16 nm. b) The scheme of the conduction band profile for negative and positive bias.

The photocurrent (PC) of the samples was also measured by Fourier transform spectroscopy as a function of applied bias. The technique is described in section 5.1. Figure 6.11 shows the spectra for the samples with 10 or 13 nm thick InP barriers. A narrow peak around 12 microns appears when the samples are positively biased. Positive bias means that the substrate has a higher potential and therefore, the electrons move towards the substrate. For all samples at zero bias a relative broad peak around 6 microns is observed, which is detailed in section 6.2.

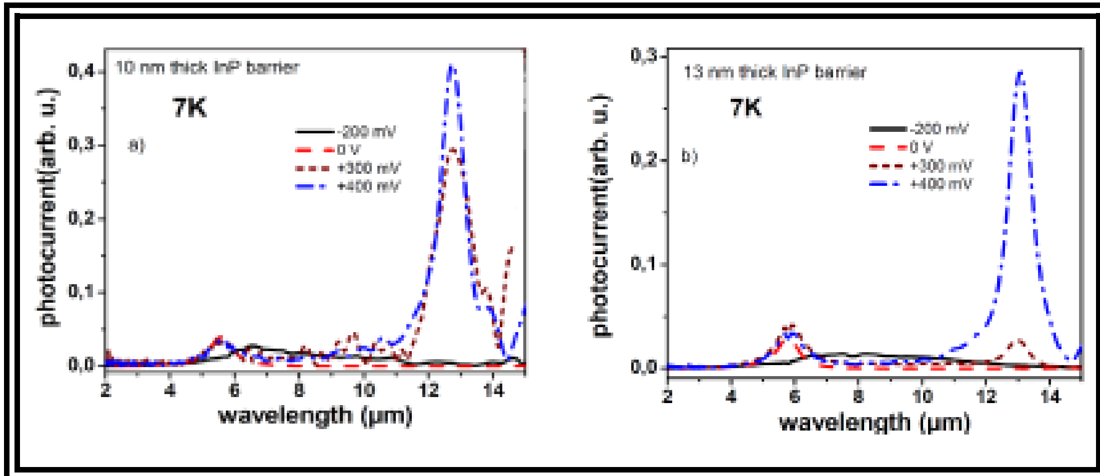

Figure 6.11: Photocurrent for the samples with 10 nm (left side) and 13 nm (right side) thick InP barrier as function of bias. For the samples a peak at 12 microns is observed at positive bias.

For the sample with the thickest InP barrier (Figure 6.12) we do not observe the narrow peak at 12 microns. For negative bias a broad peak is measured for all three samples.

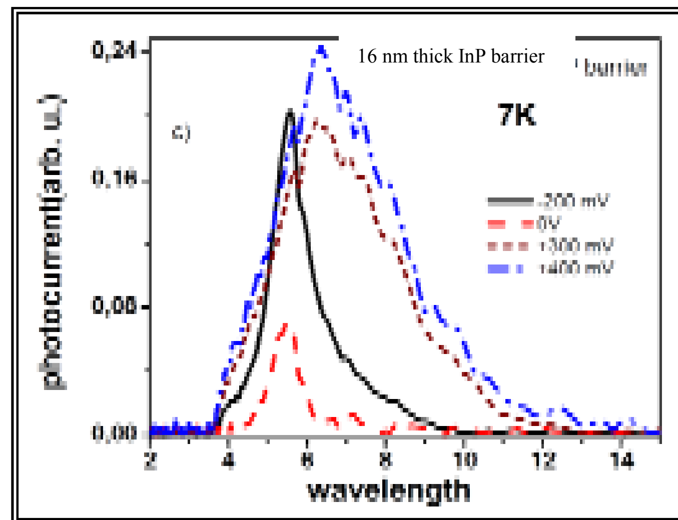

Figure 6.12: Photocurrent for the 16 nm InP barrier.

The 12 microns peak has a full width at half maximum of less than 5 meV, corresponding to a $\Delta\lambda/\lambda$ of only 5 %, indicating that a bound to bound transition is involved. To understand the observed PC we used the method described in chapter 4 to calculate the energy levels for the structures and the oscillator strengths for all possible

transitions. The most important energy levels for angular momentum quantum numbers m=0 (solid lines) and m=1 (dashed lines) are shown in figure 6.13a, superimposed on the QD structure potential profile for positive bias. For an energy of 100 meV (12 microns) the most probable transition is from the lowest energy level to the first excited state both with m = 1, namely state (0,2) to state (1,3). Figure 6.13b shows the probability density in the ρz plane, where z is the growth and ρ is the QD base radius directions, for these two states. One clearly sees that both the (0,2) and (1,3) states are fully localized in the QD. The absorption involved in the 100 meV PC peak is attributed to the optical transition between these two states. The localized nature of these energy states explains the exceptionally narrow generated peak.

In the final absorption state, the photoexcited electron has an energy about 120 meV below the InGaAlAs conduction band. In order to contribute to the current, the photoexcited electron has three possibilities, namely: 1) be transferred to the continuum, 2) to the InGaAlAs conduction band or 3) to an extended state close to it. The direct transfer of the photoexcited electron to the InGaAlAs conduction band or to the continuum, which could be eventually mediated by intraband Auger scattering, as already reported [6.11], is ruled out since the 100 meV peak is absent in equivalent samples which do not have the InGaAs quantum well and is not observed for negative bias. In fact, this peak is only observed for positive bias, as shown in figure 6.11. In the latter case, the transfer from the final absorption state to an extended state close to the conduction band of the quaternary material cannot be triggered thermally because the energy required is rather high, around 120 meV. This transfer should then occur in two steps. First the electron is excited either by an Auger [6.11] scattering process or by the absorption of a second photon to one of the many states which are predominantly localized in the quantum well, as state (0,28) for instance, as shown in figure 6.13. It should be pointed out that the calculated oscillator strength for such a transition is very high. At this point, the electron can effortlessly move to the adjacent quantum well since its wavefunction is predominantly localized there. Once in this QW-like state, the photoexcited electron can then easily reach the close by conduction band of the quaternary material by tunnelling through the inverted V-shaped barrier under a positive bias. For negative bias, these electrons would have to move in the direction of the InP barrier and that is not possible due to the thicker (InP + InGaAlAs) barrier.

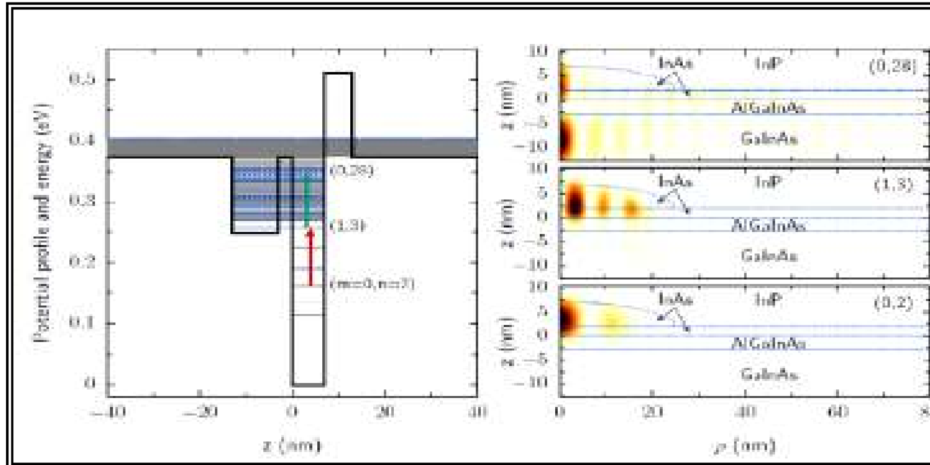

Figure 6.13: Relevant energy levels and the optical transitions with the highest oscillator strength for the 13 nm InP barrier structure.

To finalize the section, Figure 6.14 shows the detectivity for the 10 nm thick InP barrier which shows a better performance at low temperature operation.

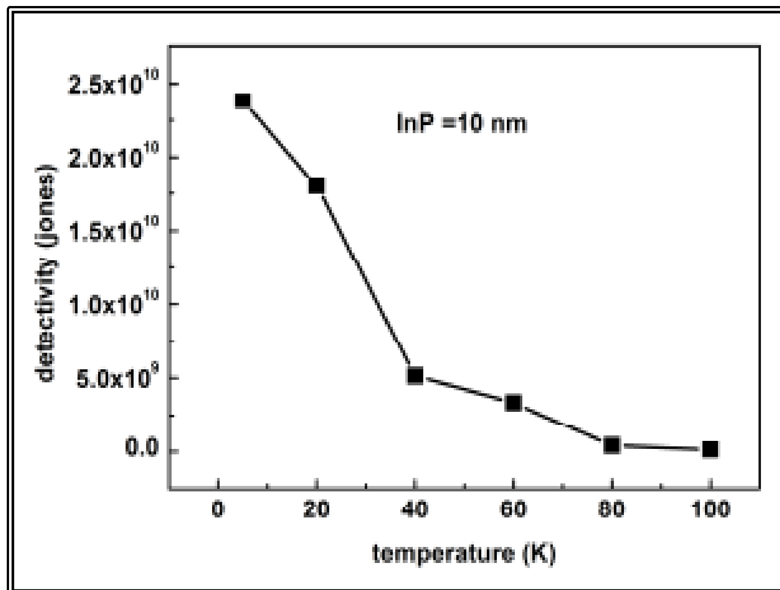

Figure 6.14: detectivity for the 10 nm thicker InP barrier as funcition of temperature.

In summary we have developed an InGaAlAs/InGaAs/InGaAlAs/InAs/InP QDIP structure which can generate an exceptionally narrow photocurrent around 12

μm. The identification of the energy levels involved in the PC generation processes was made with the help of two independent calculation methods. The energy levels involved in the absorption are fully localized in the quantum dots. In order to generate the observed photocurrent, the electrons first reach the conduction band of the quaternary material via the adjacent InGaAs quantum well either by an intraband Auger effect or by the absorption of a second photon (which mechanism is yet to be determined) and finally tunnel through the thin InP barriers. Enhanced photocurrents are expected if the QDs are covered with the quaternary material, avoiding the last tunnelling step. This would require improvements in the crystal growth of the InGaAlAs layer under a varying growth temperature.

6.4 Dual Sign Photocurrent in Quantum Dot Structures for Infrared Photodetection

The photocurrent generation in quantum dot infrared photodetectors (QDIPs) involves, at least, 4 mechanisms. First the absorption of the incident light to photoexcite a carrier, then the extraction of the carrier from the quantum dot, followed by the transport of this carrier along the structure and, finally, the collection of the carrier to generate the PC trough an external circuit [6.15]. The understanding of these mechanisms can guide us in optimizing the detectivity of a photodetector, which is directly proportional to the photocurrent intensity (responsivity). The ideal case would be 100% efficiency, where all the excited electrons are collected, contributing to the PC. It is important to mention that the responsivity of quantum dot structures for infrared photodetectors is expected to be higher when compared to quantum well structures due to the longer life time of the carriers [6.16]. In this section we investigate how the structure around the quantum dot can influence the mechanisms of carrier extraction and consequently the photocurrent signal.

For this study two different samples were analyzed. Both structures were grown lattice matched to InP substrates by metalorganic vapor phase epitaxy. On the substrate, for the first one (Sample A in Figure 6.15), an InGaAlAs material with 20% Al content was deposited. After depositing 99 nm of this quaternary, a graded layer was grown

continuously varying the Al content from 20% to 11% so as to generate a half parabolic-shaped potential well (PQW). This graded layer is kept lattice matched to the substrate by varying the In and Ga concentrations accordingly. Then a 3 nm thick layer of InGaAlAs was deposited, on top of which the InAs QDs were nucleated. An 8 nm thick layer of InP, acting as a second barrier, was used to cover the dots. The second half of the parabolic quantum well was then grown varying the Al content of the quaternary material from 11% to20%, keeping the material lattice matched. Finally 99 nm of lattice matched InGaAlAs with 20% Al was deposited completing the first period. Ten periods like this one were grown. Bottom and top electrical contact layers, made of $In_{0.53}Ga_{0.47}As$ heavily doped ($n = 2 \times 10^{18}$ cm^{-3}) were deposited as shown schematically in Fig. 6.12.

For the second structure (Sample B in figure 6.16) a lattice matched InGaAlAs layer with 20% Al was first deposited on the InP substrate, followed by a 4 nm thick $In_{0.52}Al_{0.48}As$ barrier layer. Then a 3 nm layer of lattice matched InGaAlAs also with 20% Al was grown on top of which the InAs quantum dots were nucleated and covered by 8 nm of InP. A 3 nm thick layer of $In_{0.52}Al_{0.48}As$ was then deposited on top of which an $In_{0.53}Ga_{0.47}As$ quantum well was grown. As the barrier material for the QW, a 4 nm $In_{0.52}Al_{0.48}As$ barrier layer was grown. The thin $In_{0.52}Al_{0.48}As$ barriers were grown in order to achieve lower dark current. Finally, a 99 nm layer of 20%Al, lattice matched InGaAlAs was deposited, to complete the first period. As for sample A, this structure had ten periods sandwiched between $In_{0.53}Ga_{0.47}As$ heavily doped ($n = 2 \times 10^{18}$ cm^{-3}) contact layers.

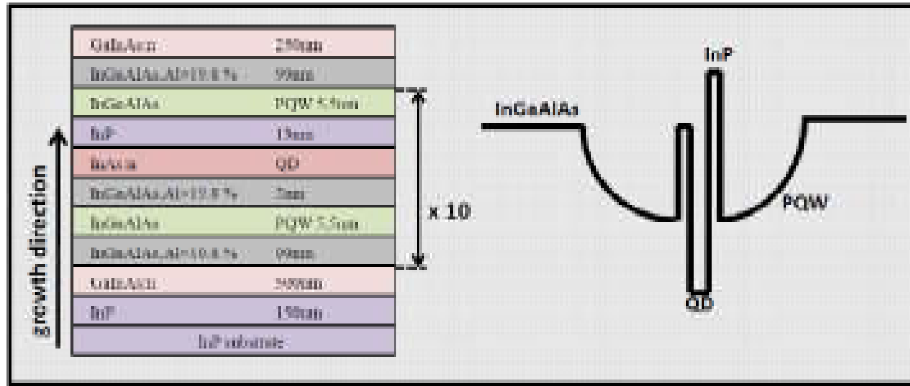

Figure 6.15: Schematic diagram of the layer sequence and conduction band profile of Sample A. On the left hand side the material composition and the thickness of each layer is specified.

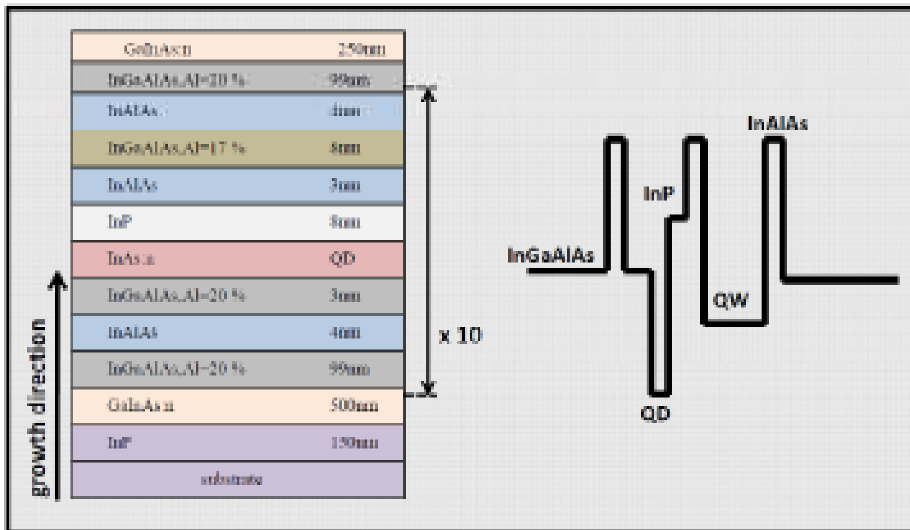

Figure 6.16: Schematic diagram of the layer sequence and conduction band profile of Sample B. On the left hand side the material composition and the thickness of each layer is specified.

The photocurrent response was measured with Fourier transform infrared spectroscopy (FTIR) as a function of bias and temperature (Chapter 5). The *current versus voltage* curves were performed with a parametric analyzer.

Figure 6.17 shows the PC spectrum of Sample A measured at low temperature and as a function of the external applied bias. Here, again, positive bias means that the electric field points from the bottom of the structure to the top. For high positive biases the PC response shows a strong peak centered at 240 meV. For negative biases a much broader peak around 180 meV, which is already present at positive bias, grows rapidly

in intensity and dominates the spectrum for the highest bias values. Close to zero bias, photocurrent in both directions is observed, at different values of photon energy. This dual behavior was also studied by Schneider in a previous work on quantum well structures [6.17-6.19] and it was shown to be related to the asymmetry in the structure. In our case, the InP barrier, that covers the QDs, promotes a preferential escape direction for the electrons that is in the opposite direction of the barrier, since the tunneling probability is not so high.

To make a detailed study of this behavior a second structure was developed (Figure 6.16). In this one we included a quantum well after the InP barrier. The PC spectra of the sample as a function of the external applied bias voltage at low temperature are shown in Figure 6.18. Two narrow and intense peaks, one at 190 meV and a second one at 230 meV can be clearly identified. A third, weaker peak, is observed at 300 meV. As the external bias voltage is decreased, for values very close to zero bias the same dual sign photoresponse, as seen in Sample A, is measured. For the same value of external applied bias voltages, current flows in both directions.

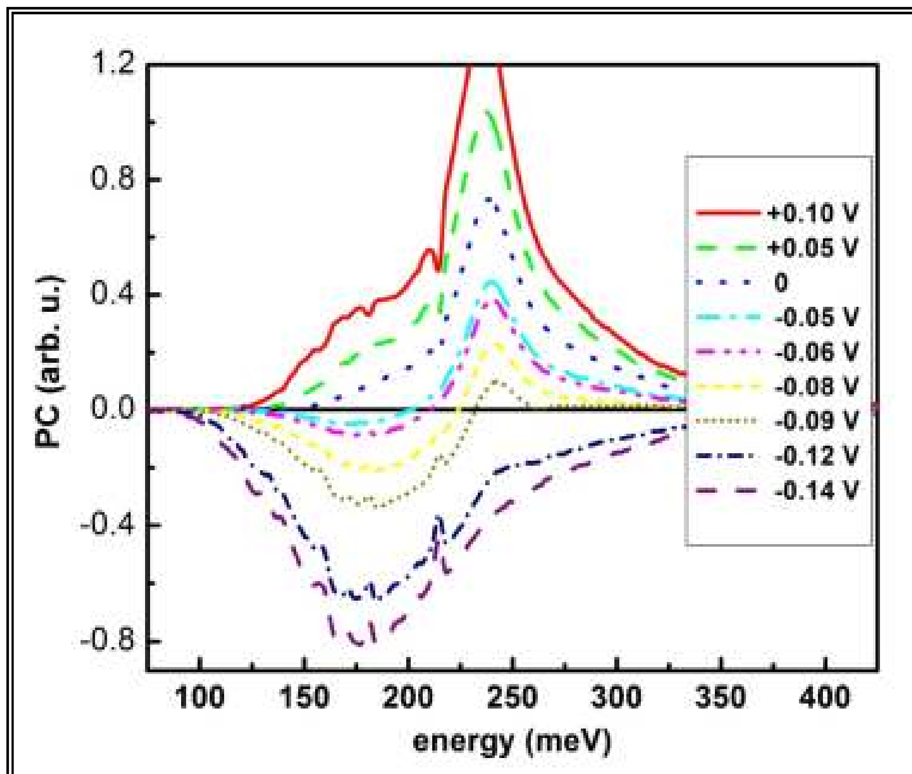

Figure 6.17: PC spectrum for sample A as a function of the external applied bias voltages.

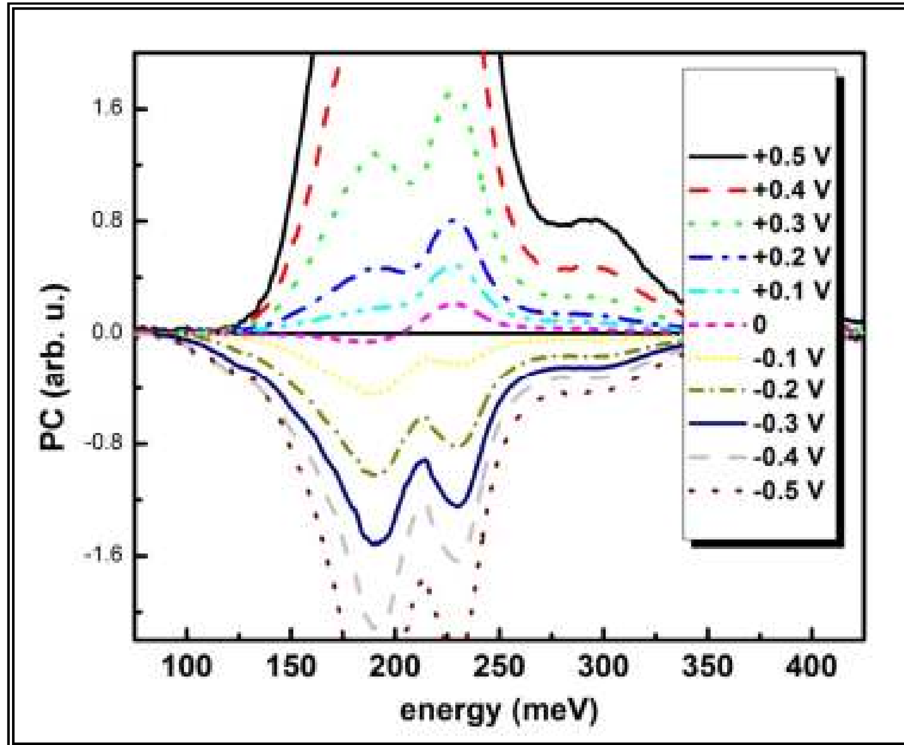

Figure 6.18: PC spectrum for sample B as a function of the external applied bias voltages.

To explain the results full three dimensional numerical calculations of the energy levels and transition oscillator strengths were performed in the envelope function approximation (Chapter 4). From this we are able to assign each PC peak to a particular transition. In Figures 6.19a and 6.20a the conduction band profile of the structure and the calculated energy levels are depicted. The arrows in the figures indicate the transitions with the highest oscillator strength. Figures 6.19b and 6.20b show all the calculated oscillators strength, superimposed on the PC measurements. In this graph different symbols mean different initial energy state transitions. In Sample A the measured PC is due to a transition from a bound state in the QD to a state close to the band edge of the quaternary material. For zero bias the electron has a higher escape probability to the left side due to the asymmetric barriers originating the PC peak centered at 240 meV. When the sample is negatively biased the InP potential barrier is decreased and PC in both directions is measured. The low energy transition increases with negative bias due to charge accumulation in the quantum dot.

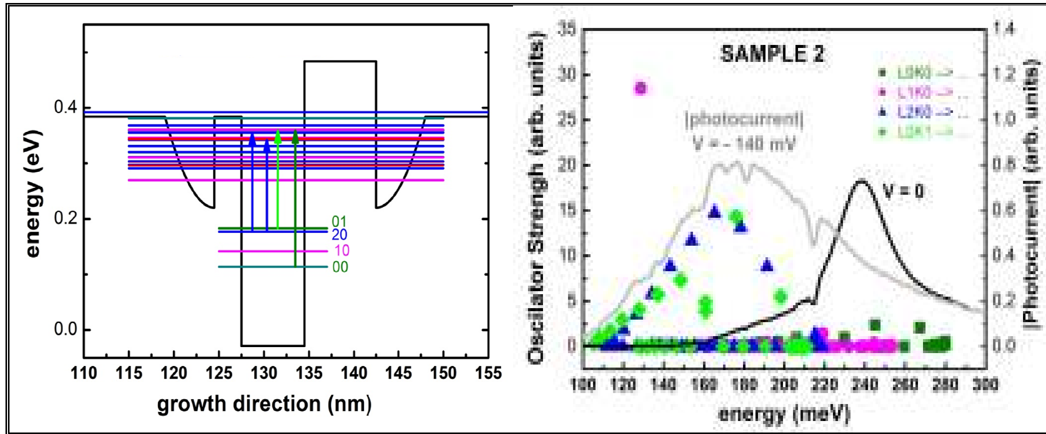

Figure 6.19: Some of the calculated energy levels for sample A. The thin arrows represent the transitions responsible for the photocurrent generation.

In sample B, the low energy PC peak at 190 meV is attributed to a transition between an excited state of the QD to a state extended to the QW. The high energy PC peak, at 230 meV, is attributed to a transition from the ground level to a state above the InGaAlAs band edge. The weaker one, at 300 meV, is a transition to the quasi-continuum. An electron in a final energy state of the 230 meV transition has higher probability of tunneling to the left, due to smaller potential barrier and an electron in a final energy state of the low energy transition is resonant transferred from final energy state to a state centered in the neighboring quantum well.

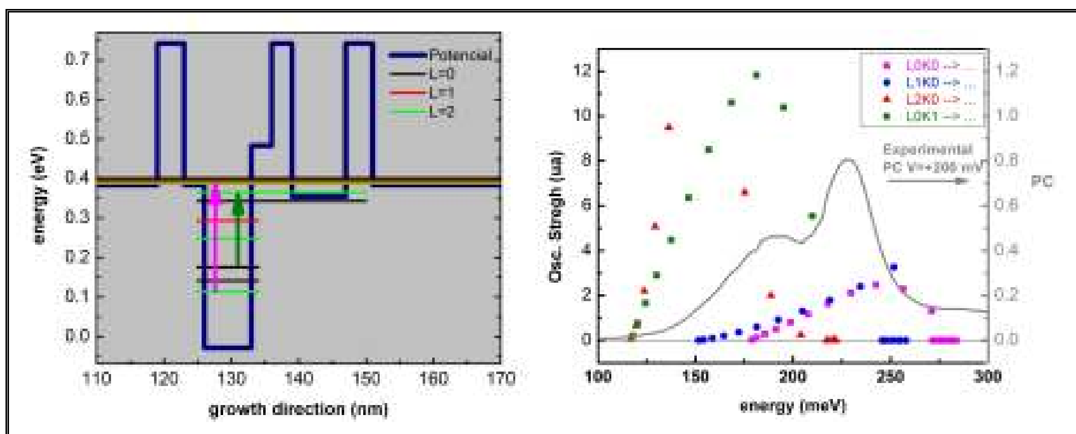

Figure 6.20: Some of the calculated energy levels for sample B. The thin arrows in the quantum dot region represent the transitions with highest oscillator strength.

The carrier extraction mechanisms, under small or no external applied bias conditions, depend on the designed structure. The presence of the barriers in these QDIP structures is essential not only to provide higher dot homogeneity but also to block electrons which are thermally generated (dark current). The drawback of the barriers is that they also block the signal (photocurrent). Analyzing these structures one can conclude that the quantum well potential suppresses the barrier effect, providing a way to extract the photogenerated carriers from the quantum dots.

Figure 6.21 shows the IV curves for sample B. The curves are asymmetric as a consequence of the asymmetry of the structure. The lower dark current happens for positive bias. The inset shows a zoom close to zero bias and the curves are shifted towards positive bias voltages. This built in field is also due to the asymmetry in the structure and tell us that the lower dark current is not at zero bias.

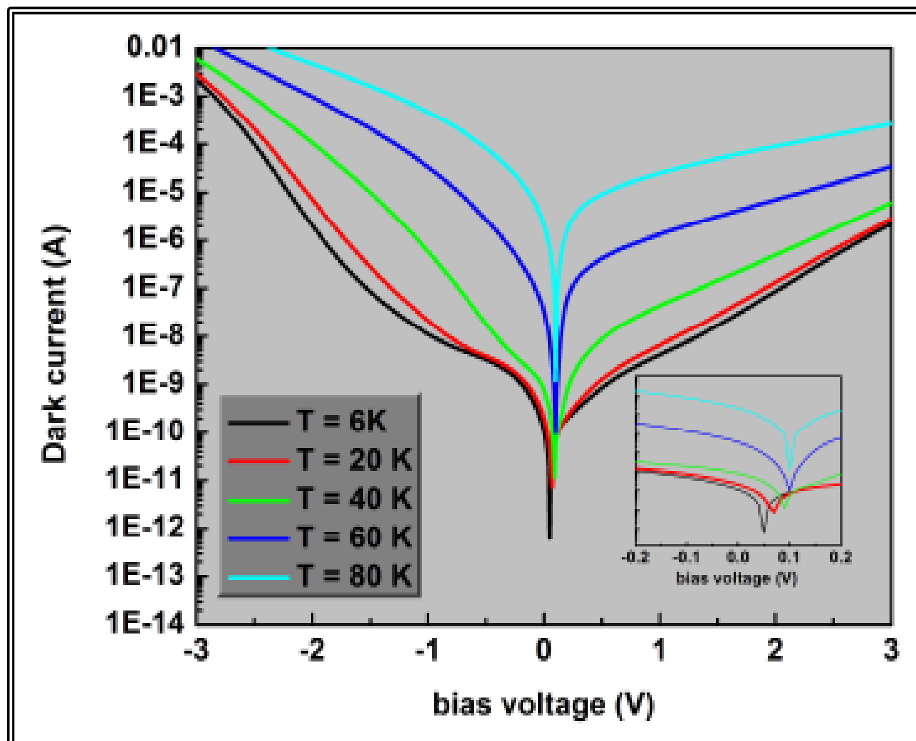

Figure 6.21: Voltage-current curves as function of temperature for Sample B. The inset shows a zoom close to zero bias voltages.

To summarize, we showed that different carrier extraction mechanisms in quantum dot infrared photodetector structures will reinforce different transitions resulting in different photoresponses. We also show that the carrier extraction

mechanisms can be altered by the design of the structure. The negative and positive photoresponse at the same applied bias, and different wavelengths, can be obtained by designing asymmetric quantum dot structures, due to different carrier extraction mechanisms.

References

[6.1] J. S. Kim, P. W. Yu, J. Lemm, M. Jeon, S. K. Noh, J. I. Lee, G. H. Kim, S. Kang, J. S. Kim, S. G. Kim, *J. Appl. Phys*. **91**, 5055 (2002).

[6.2] S. Krishna, S. Raghavan, G. von Winckel, P. Rotella, A. Stintz, C. P. Morath, D. Le e S. W. Kennerly, *Appl. Phys. Lett*. **82**, 2574 (2003).

[6.3] G. Ariyawansa, A.G.U.Perera, X.H.Su, S. Chakrabarti, P. Bhattacharya, *Infrared Physics and technology* **50**, 156 (2007).

[6.4] Lim H, Zhang W, Tsao S, Sills T, Szafraniec J, Mi K, Movaghar B, Razeghi M, *Phys. Rev. B* **72**, 085332 (2005).

[6.5] Liu H C, *Opto-electronics Rev*. **11**, 1 (2003).

[6.6] Boucaud P, Sauvage S*, C. R. Physique* **4**, 1133 (2003).

[6.7] Towe E, Pan D, IEEE J. Sel. *Topics Quantum Electronics* **6**, 408 (2000).

[6.8] Pan J L, Phys Rev. B **49**, 11272 (1994).

[6.9] Landin L, Pettersson H, Kleverman M, Borgström M, Zhang X, Seifert W and Samuelson L, *J. Appl. Phys*. **95**, 8007 (2004).

[6.10]Nilsson H H, Zhang J Z, Galbraith I, *Appl. Phys. Lett*. **91**, 161113 (2007).

[6.11] T. Gebhard et al, *Appl. Phys. Lett* 93, 052103 (2008)

[6.12] Borgström M, Pires M P, Bryllert T, Landi S M, Seifert W, Souza P L, *Journal of Crystal Growth* **252**, 481 (2003).

[6.13]Souza P L, Gebhard T, Lopes A J, Pires M P, Villas-Boas J M, Unterrainer K, Guimarães P S S, Vieira G S and Studart N, *Appl. Phys. Lett*. **90**, 173510 (2007).

[6. 14] Müller T, Schrey F F, Strasser G, and Unterrainer K, Appl. Phys. Lett. **83**, 3572 2003

[6.15] P. Bhattacharya, Semiconductor Optoelectronic devices, 2nd Edition, Prentice Hall, 1997

[6.16] H. Lim et al, *Appl. Phys. Lett.* **90**, 131112-1 (2007)

[6.17] H. Schneider et al, *Appl. Phys. Lett.* **60** 1471 (1992)

[6.18] H. Schneider et al, *Superlattices and Microstructures* **23**, 1289 (1998)

[6.19] C. Schönbein et al, *Appl. Phys. Lett*. **68**, 973 (1996)

7. SUMMARY AND CONCLUSIONS

In this thesis I present a study on new structures and materials for infrared photodetection, with the aim of developing high performance Quantum Dot Infrared Photodetectors (QDIPs). We designed structures based on self-assembled InAs quantum dots grown by Metalorganic Chemical Vapor Deposition (MOCVD) on InP substrates. We focus our study on the physical properties of these structures, especially on the mechanisms involved to generate a photocurrent. To characterize the devices, photocurrent measurements were performed using Fourier Transform Infrared Spectroscopy (FTIR). These measurements were done as function of temperature and external applied bias voltage. Complementary characterizations techniques, such as current-voltage and optical absorption measurements, and theoretical modeling were also performed to achieve a better understanding of the mechanisms behind these devices.

In section 6.2 we show that intraband Auger processes can play an important role in generating the photocurrent in InAs/InP based QDIPs. Theoretical calculations show that the photocurrent peak is due to a bound to bound transition in the quantum dot with the final state of the transition being around 200 meV below the continuum of energy states of the structure. Temperature dependence photocurrent, optical absorption and photoluminescence measurements strongly support the proposed model that an Auger effect plays an important part in the photocurrent generation.

In section 6.3 we demonstrate a QDIP structure which operates around 12 microns with a photocurrent peak as narrow as 4.5 meV, desirable for achieving high selective devices. The peak is attributed to photon absorption between InAs quantum dot bound states, followed by a carrier extraction mechanism where the coupling to the adjacent InGaAs quantum well is highlighted. The possible role played by intraband Auger scattering, multi-photon sequential absorption and tunneling in generating the observed current peak is also addressed.

In section 6.4 we investigate how the layers around the quantum dot can influence the carrier extraction and consequently the photocurrent signal. We present QDIP structures which display negative and positive photoresponses for the same

applied bias and for different wavelengths. This dual behavior is a consequence of different carrier extraction mechanisms.

In summary, we have studied the physical properties of quantum dots and QDIPs, especially the effect of the carrier extraction mechanisms, with the aim to produce high efficient devices.